JOURNAL OF GEOPHYSICAL RESEARCH, VOL. 114, D06110, doi:10.1029/2008JD010662, 2009

Relative intensities of middle atmosphere waves

D. Offermann,[1] O. Gusev,[1,2] M. Donner,[3] J. M. Forbes,[4] M. Hagan,[5] M. G. Mlynczak,[6] J. Oberheide,[1] P. Preusse,[7] H. Schmidt,[8] and J. M. Russell III[9]

Received 25 June 2008; revised 6 January 2009; accepted 21 January 2009; published 21 March 2009.

[1] Climatologies of gravity waves, quasi-stationary planetary waves, and tides are compared in the upper stratosphere, mesosphere, and lower thermosphere. Temperature standard deviations from zonal means are used as proxies for wave activity. The sum of the waves is compared to directly measured total temperature fluctuations. The resulting difference is used as a proxy for traveling planetary waves. A preliminary climatology for these waves is proposed. A ranking of the four wave types in terms of their impact on the total wave state of the atmosphere is achieved, which is dependent on altitude and latitude. At extratropical latitudes, gravity waves mostly play a major role. Traveling planetary waves are found to play a secondary role. Quasi-stationary planetary waves and tides yield a lesser contribution there. Vertical profiles of total temperature fluctuations show a sharp vertical gradient change ("kink" or "bend") in the mesosphere. This is interpreted in terms of a change of wave damping, and the concept of a "wave turbopause" is suggested. The altitude of this wave turbopause is found to be mostly determined by the relative intensities of gravity waves and planetary waves. The turbopause is further analyzed, including earlier mass spectrometer data. It is found that the wave turbopause and the mass spectrometer turbopause occur rather close together. The turbopause forms a layer about 8 km thick, and the data suggest an additional 3 km mixing layer on top.

Citation: Offermann, D., O. Gusev, M. Donner, J. M. Forbes, M. Hagan, M. G. Mlynczak, J. Oberheide, P. Preusse, H. Schmidt, and J. M. Russell III (2009), Relative intensities of middle atmosphere waves, *J. Geophys. Res.*, *114*, D06110, doi:10.1029/2008JD010662.

1. Introduction

[2] Various types of waves exist in the middle atmosphere (MA, 10–100 km). They are observed in atmospheric pressure, temperature, density, wind, and trace gas mixing ratios. Very long as well as very short scales exist in their periods and their wavelengths. Amplitudes can be very large: in temperature, for instance, they can exceed 25% of the large-scale mean values (e.g., 57 K [*Offermann et al.*, 2006a]). In consequence the atmospheric behavior as a whole cannot be understood if the waves are not taken into account. In the present paper we therefore study MA waves as seen in the temperature.

[3] A number of climatologies for atmospheric temperatures have been developed in the past as for instance the CIRA, Mass Spectrometer and Incoherent Scatter Radar (MSIS), and NRLMSISE-00 empirical models [*Fleming et al.*, 1990; *Hedin*, 1983; *Picone et al.*, 2002]. They are based on previous satellite and auxiliary data. Recently more than 4 years of Sounding of the Atmosphere using Broadband Emission Radiometry (SABER) measurements on the Thermosphere, Ionosphere, Mesosphere, Energetics, and Dynamics (TIMED) satellite have become available [e.g., *Mertens et al.*, 2001, 2004]. Reviews on temperature measurements and temperature trends in the stratosphere and mesosphere have been given by *Ramaswamy et al.* [2001] and *Beig et al.* [2003, see also references therein].

[4] Atmospheric waves have generally not been considered in the development of middle atmosphere temperature climatologies. One exception is *Rees*'s [1990] empirical model (CIRA 1986) that contains a climatology of stationary planetary waves from *Rees* [1990]. More recently, climatologies have been developed for migrating and nonmigrating tides and stationary planetary waves [*Forbes et al.*, 2008] and for gravity waves [*Preusse et al.*, 2009]. These data sets will be used in the present paper. Temperature climatologies of tidal waves have only recently become available from SABER data [i.e., *Forbes et al.*, 2008] and thus we adopt monthly tidal amplitudes from the Global Scale Wave Model [*Hagan et al.*, 1999; *Hagan and Forbes*, 2002, 2003].

---

[1] Physics Department, University of Wuppertal, Wuppertal, Germany.
[2] Deutsches Zentrum für Luft-und Raumfahrt, Oberpfaffenhofen, Germany.
[3] Donner Tontechnik, Remscheid, Germany.
[4] Aerospace Engineering Sciences, University of Colorado, Boulder, Colorado, USA.
[5] High Altitude Observatory, NCAR, Boulder, Colorado, USA.
[6] NASA Langley Research Center, Hampton, Virginia, USA.
[7] Institut für Chemie und Dynamik der Geosphäre I: Stratosphäre, Forschungszentrum Jülich, Jülich, Germany.
[8] Max Planck Institute for Meteorology, Hamburg, Germany.
[9] Center for Atmospheric Sciences, Hampton University, Hampton, Virginia, USA.

0148-0227/09/2008JD010662

[5] Fluctuations of atmospheric temperatures can be quite strong and show systematic variations. Hence they are not noise but rather the result of superposition of various waves. Fluctuation climatologies have been presented long ago by *Cole and Kantor* [1978] and *Chanin et al.* [1990]. Fluctuations of Limb Infrared Monitor of the Stratosphere (LIMS) and Microwave Limb Sounder (MLS) temperatures have been interpreted in terms of gravity waves by *Fetzer and Gille* [1994] and *Wu and Waters* [1996], respectively. Further analyses on the basis of Cryogenic Infrared Spectrometers and Telescopes for the Atmosphere (CRISTA) and SABER measurements are given by *Offermann et al.* [2006a, see also references therein].

[6] In the present paper we discuss the major wave types including gravity waves GW, quasi-stationary planetary waves, and tides, in sections 2 and 3. The intensities of each of these wave types are compared in section 4. The effects of tides, gravity waves, and stationary planetary waves are added and compared to that observed by SABER. Differences are then interpreted as because of planetary waves and a "climatology" for these waves is attempted in section 4.

[7] The vertical profiles of measured fluctuation intensities (temperature standard deviations) exhibit a kink or bend in the upper mesosphere. This has been interpreted in terms of wave damping by *Offermann et al.* [2006a, 2007]. The kink has been named the "wave turbopause" in these papers. The wave turbopause has been found in similar form in different data sets (CRISTA and SABER measurements, Hamburg Model of the Neutral and Ionized Atmosphere (HAMMONIA) model calculations). It was found that the altitude at which the turbopause occurs can vary considerably. The variations depend on latitude and season, and the seasonal variations are latitude dependent. These results have recently been checked and confirmed by an independent data set and analysis [*Hall et al.*, 2008]. The detailed reason for the bent structure of the vertical profiles has not been given by *Offermann et al.* [2006a, 2007]. It will be attempted here by analysis of the profile shapes of the various wave types (section 5). In section 6 the results are discussed with respect to wave energy density, traveling planetary waves, and the wave turbopause. Conclusions are drawn in section 7.

2. Data

[8] Since 2002 the SABER instrument on the TIMED satellite has measured – and still measures, a wealth of temperature data in the middle atmosphere up to about 120 km. These data can be used for the analysis of middle atmosphere waves. The wave intensity can be quantified by the standard deviation σ from the mean temperature T, or by its square σ^2, with σ given by the wave amplitude divided by the square root of two. A superposition of waves can hence be described by the square root of the sum of squared standard deviations of the various waves, assuming the waves are random

$$\sigma_{\mathrm{sab}}^2 = \sigma_{\mathrm{gw}}^2 + \sigma_{\mathrm{M}}^2 + \sigma_{\mathrm{spw}}^2 + \sigma_{\mathrm{tide}}^2. \quad (1)$$

[9] Here the index denotes the different waves: gw is gravity waves, M is traveling planetary waves, spw is stationary planetary waves, and tide is tidal waves. For a given temperature field the quantity σ_{sab} is basically the fluctuation intensity of that field. As σ_{sab} is easily calculated in a given field we will use it as a proxy for wave activity throughout this paper. It is very suitable for comparison of different waves. We use zonal bands of data at a given latitude with a latitudinal width of 10° every 10°. The mean temperature in each band is calculated on a monthly basis including 4 years of data, and σ_{sab} is the standard deviation of the data from this mean.

[10] This method has been extensively used by *Offermann et al.* [2006a, 2007, see also other references therein]. Data accuracy has been discussed in detail by *Offermann et al.* [2006a]. (Instrument noise is negligible in the present context for V1.04 and V1.06 SABER data [see *Offermann et al.*, 2006a; *Oberheide et al.*, 2006a].)

[11] An example is shown in Figure 1 in which the altitude/latitude distribution of temperature standard deviations (σ_{sab}) as measured by the SABER instrument are given for the month of July. Mean values for 4 years of data (SABER data Version 1.06 from 2002 to 2005) are presented. Note that above 100 km the algorithm used to derive SABER temperature requires atomic oxygen that is specified using the NRL-MSISE00 model. In addition the region above 100 km is subject to large variations due to the sensitivity to solar ultraviolet flux and geomagnetic conditions. These issues do not affect the present analysis that is mostly restricted to below 100 km. Figure 1 shows pronounced structures including a large summer-winter difference at lower altitudes and a steep increase with altitude from low to high values at high altitudes in both hemispheres.

[12] If one takes a vertical cut through Figure 1 at a given latitude (for instance 40°N) one obtains the curve shown in Figure 2 (green line, year 2002). We also use CRISTA data here as a link to *Offermann et al.* [2006a, 2007] and show for comparison a profile from the CRISTA 2 measurements (black curve [*Offermann et al.*, 2007]). Corresponding results from HAMMONIA model calculations [see *Schmidt et al.*, 2006; *Offermann et al.*, 2007] are also shown (red line). HAMMONIA is a general circulation and chemistry model extending from the surface to the thermosphere. The results presented here are from an arbitrarily chosen year of a 20-year simulation for present-day solar minimum conditions described by *Schmidt et al.* [2006]. The three profiles in Figure 2 are in approximate agreement which is quite encouraging. Each of them appears to consist of two parts: one with a moderate positive gradient at the lower altitudes, and one with a steep gradient at the upper altitudes. This is illustrated by the two straight lines (blue) which are fits (to the SABER data) in the altitude regions 40–75 km and 95–110 km, respectively. The two lines intersect at about 90 km (square in Figure 2) where each of the profiles appears to have a "kink" or a "bend." This profile structure has been attributed to differences in wave dissipation at the lower and upper altitudes, and the kink has been denoted as the wave turbopause [*Offermann et al.*, 2006a, 2007]. It will be further discussed in sections 5 and 6.3.

[13] In the subsequent parts of this paper vertical profiles of wave intensity will be shown for various types of waves. Many of them show a kink structure like that in Figure 2. The major waves in the middle atmosphere are gravity

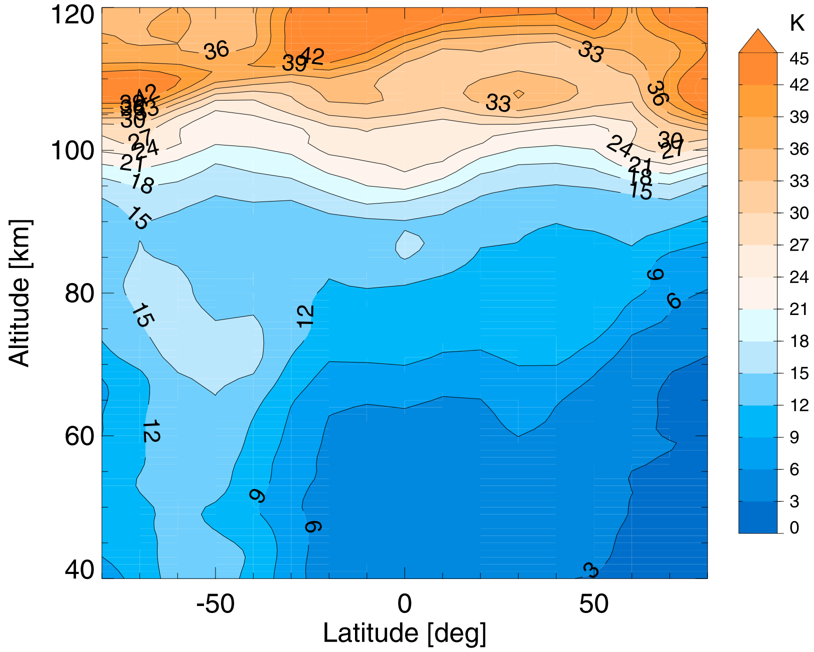

Figure 1. Temperature standard deviations σ_{sab} from zonal mean temperatures (SABER version 1.06) are shown for July. Mean values are given for years 2002–2005. Isoline spacing is 3 K.

waves, traveling planetary waves, stationary planetary waves, and tides. Their intensities depend on altitude and latitude. In principle they all can be present at a given place simultaneously. It is therefore difficult to disentangle their superposition and to determine their relative importance. Recently, however, a number of wave climatologies have been developed. They will be used here to estimate the relative intensities of these waves.

2.1. Gravity Waves

[14] Preusse and collaborators have developed a gravity wave climatology on the basis of more than 4 years of SABER data (2002–2006, version 1.06 [*Krebsbach and Preusse*, 2007; *Preusse et al.*, 2009]). Altitude profiles of SABER temperatures are detrended by subtracting a wave number 0–6 background atmosphere estimated by a Kalman filter [*Preusse et al.*, 2002]. In this way gravity waves are isolated from the zonal mean, planetary waves, and the signatures of breaking planetary waves [*Ern et al.*, 2006]. Tidal signatures are removed by detrending the data separately for ascending and descending orbit lags [*Preusse et al.*, 2001].

[15] Residual temperatures are analyzed by a combination of the maximum entropy method applied to the entire profiles and subsequent sinusoidal fits in a 10 km wide running window. The analysis results in amplitude, phase, and vertical wavelength of the two leading wave components. Zonal means for various altitudes and latitude bins are calculated as RMS values.Wave amplitudes depend on altitude and latitude. Analyzed vertical wavelengths are between 5 and 30 km. Resulting climatotlogies agree favorable with dedicated GW modeling and support the interpretation of temperature residuals in terms of GWs [e.g., *Eckermann and Preusse*, 1999; *Ern et al.*, 2006; *Preusse et al.*, 2009]. It should be noted that a limb-scanning instrument with a limited altitude resolution like SABER (2 km) has difficulties in measuring waves with wavelengths shorter than this [see *Preusse et al.*, 2002]. The short wavelength part of the gravity wave spectrum is therefore not contained in the climatology. It means that the sum of the amplitudes or the standard deviations used here are lower limits. This needs to be kept in mind during the subsequent discussions, though the contribution of

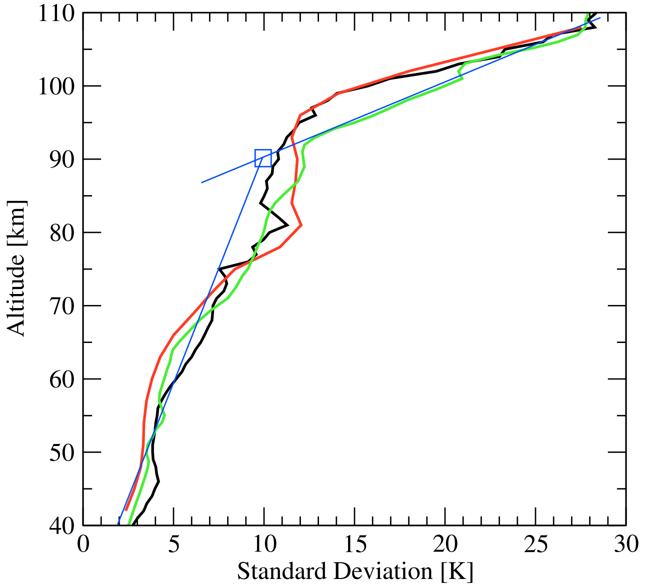

Figure 2. Vertical profiles of temperature standard deviations σ_{sab} from SABER (2002, green line) and CRISTA (1997, black line) measurements and HAMMONIA model calculations (red line). Data are for August at 40°N. Faint straight lines (blue) are fits to the lower and higher-altitude SABER data (see text for details).

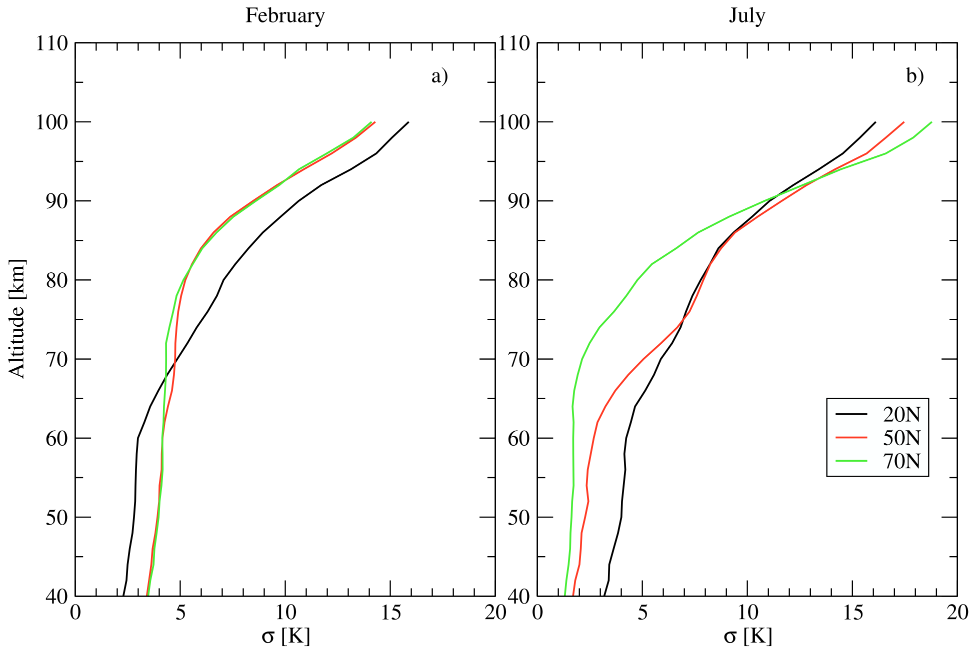

Figure 3. Gravity wave climatology for (a) winter (February) and (b) summer (July). Latitudes shown are 20 (black), 50 (red), and 70°N (green). Wave amplitudes are represented by the standard deviations σ_{gw} (see text).

waves with vertical wavelengths shorter than 5 km should be small in the mesosphere [e.g., *Smith et al.*, 1987; *Ern et al.*, 2006].

[16] Observable short horizontal wavelengths are limited by the integration along the line of sight. The limit varies with vertical wavelength and the relative orientation of the horizontal wave vector with respect to the line of sight [*Preusse et al.*, 2002, 2008]. Typical waves with horizontal wavelengths longer than 100–200 km are visible. The upper limit of the horizontal wavelength is zonal wave number 7, since the Kalman filter removes wave numbers 6 and lower. However, for the stratosphere CRISTA data indicate [*Ern et al.*, 2004; *Preusse et al.*, 2006] that GWs are limited in maximum horizontal wavelength by the ratio of the intrinsic wave frequency omega and the Coriolis parameter f: omega/f > 1.4, inducing an upper limit of the horizontal wavelength of several thousand kilometers depending on vertical wavelength and latitude [*Ern et al.*, 2006]. An overview of the observable range by limb sounding instruments is provided by *Preusse et al.* [2008].

[17] Examples from the climatology are given in Figure 3 for the months of February and July at the latitudes of 70°N, 50°N, and 20°N. The profile shapes are typical of the other months of the year. To make the picture comparable to Figure 2 the standard deviations of the gravity waves σ_{gw} are shown instead of the amplitudes. The values are somewhat smaller than in Figure 2. This indicates that waves other than gravity waves are present additionally in Figure 2. The restrictions concerning the detectability of short wavelength gravity waves also apply to the data shown in Figures 1 and 2 as they were measured by the same technique. Hence short waves are not the reason for the differences of Figures 2 and 3. The standard deviations in Figures 1 and 2 are lower limits for the same reasons discussed for the gravity waves, i.e., the limited vertical resolution of the limb sounding technique. The profiles shown in Figure 3 extend up to 100 km. The climatology does not contain data at higher altitudes. In consequence fitted lines like those in Figure 2 cannot be calculated in Figure 3. Nevertheless the profiles show a kink-like structure as their vertical gradients are flat at the lower altitudes, and are much steeper at the higher altitudes. This is especially pronounced at middle to high latitudes.

2.2. Stationary Planetary Waves

[18] Figure 4 illustrates results of an analysis of stationary planetary waves (SPW) that have recently been obtained from 1 year of SABER data (version 1.06, September 2003 to September 2004). The method uses a two-dimensional Fourier analysis (in space and time) on 60-day running mean values. The basic method has been given by *Forbes et al.* [2008]. Amplitudes and phases are available as a function of altitude and latitude for zonal wave numbers 1 to 4. As an example, Figure 4 shows the corresponding vertical profiles for the months of February and July and the latitudes of 70, 50, and 20°N. The sum of the four wave numbers 1–4 is given in this picture. It is calculated as the sum of the squared amplitudes, taking the square root of this sum (RMS). The basic assumption here is that the four waves mostly are superimposed in an incoherent manner. To obtain the standard deviations the amplitude sums are divided by square root 2 in Figure 4.

[19] Figure 4 shows large differences in wave intensity at different latitudes and times of the year, with very high values in northern winter. In northern summer the values are much smaller, which is discussed in section 4.

2.3. Tides

[20] As mentioned in section 1, a SABER based tidal climatology has only recently become available (and only

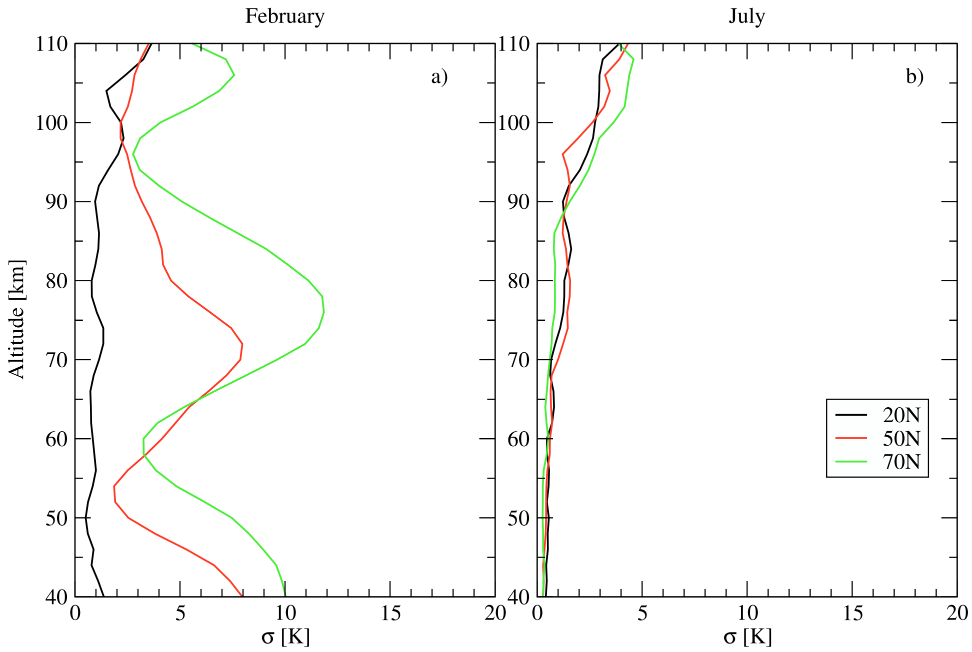

Figure 4. Stationary planetary waves for (a) winter (February) and (b) summer (July). Latitudes shown are 20 (black), 50 (red), and 70°N (green). Wave amplitudes are represented by their standard deviations σ_{spw}. Details are given in text.

between 50°S and 50°N). To represent the tides we therefore use here tidal definitions from the Global Scale Wave Model (GSWM) in its most recent version that contains a total of 26 tidal components (13 diurnal and 13 semidiurnal, with one migrating and twelve nonmigrating components for each frequency [*Hagan et al.*, 1999; *Hagan and Forbes*, 2002, 2003]). As a linear tidal model GSWM does not account for tides that are forced by nonlinear wave-wave interactions. It only includes tidal components forced by solar irradiance absorption and latent heat release in the tropical troposphere associated with deep convection activity. Hence the tidal wave intensities given in Figures 5, 6, and 8 and section 4 must be considered as lower limits. A first cross check with the new SABER based climatology, however, indicates that using the model tides does not change the results very much and leaves the basic findings of the present work unaffected.

[21] Any instrument on board a satellite in a slowly precessing orbit such as SABER observes tidal waves in the local solar time frame and not in the Universal time frame. To account for this and to make the tidal standard deviations given in Figures 5, 6, and 8 and section 4 directly comparable to the total fluctuations observed by SABER, we have computed the model tidal perturbations at the locations and times of the SABER observations ("flying the satellite through the model"). For details of the sampling method see *Oberheide et al.* [2003]. The tidal standard deviations are then derived from the sampled model data set.

[22] Examples for vertical profiles are shown in Figure 5 for the latitudes of 70°N, 50°N, and 20°N in the months of February and July. The tidal wave intensities are given as standard deviations σ_{tide}. They are relatively small when compared to the other waves. Only in the tropics and subtropics the amplitudes become large (not shown). The 20°N February profile shows a kink structure in the vertical, as indicated by the two fitted lines. This is frequently seen in the profiles, if the amplitudes are not too small (see some of the other profiles in Figure 5). In the present paper we restrict ourselves to latitudes 20–70°N. The tidal contributions to our analyses are therefore rather small.

2.4. Traveling Planetary Waves

[23] As a general test of equation (1) and of our method to derive a global climatology of traveling planetary waves (sections 3 and 4) we first use traveling planetary-scale disturbances (planetary waves, PW) that have been observed at the local station of Wuppertal (51°N, 7°E) using ground based measurements of mesopause OH temperatures [*Offermann et al.*, 2006b, and references therein]. The OH spectrometer measures the temperature at about 87 km at a time resolution of a few minutes during all nights of the year with suitable weather. The data for each night are averaged. Thus gravity wave signatures are mostly excluded. Gravity waves are also suppressed because the light emitting OH layer is about 8 km thick in the vertical, and therefore short wavelength waves cancel to a large degree in the measurements. The resulting nightly mean data still vary strongly during the course of the year and on a time scale of days. To separate the two different types of variations a harmonic fit to the data is calculated allowing for an annual, a semiannual, and a terannual component. This fit is subtracted from the nightly data, and thus the major part of data variance is removed from the data set. The resulting residues still show a considerable variability (up to ±15 K). This has been analyzed, for instance, by *Bittner et al.* [2000, 2002], and has been interpreted as planetary waves with periods of a few days to weeks.

[24] The standard deviations of these residues are therefore taken as a measure of the planetary wave amplitudes. As the planetary waves are estimated from the temporal variations at

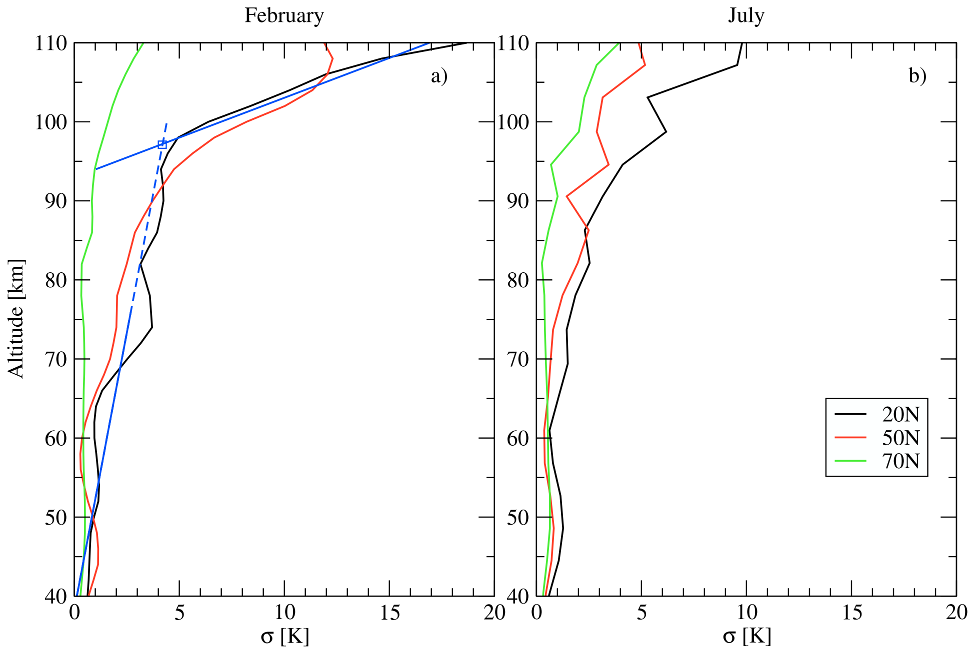

Figure 5. Tidal wave amplitudes as represented by their standard deviations for (a) February and (b) July. Latitudes shown are 20 (black), 50 (red), and 70°N (green). Data are taken from the Gobal Scale Wave Model and include 26 migrating and nonmigrating wave components (see text). Blue lines in Figure 5a are fits to the 20°N data.

a fixed location the data should not see much influence from the (fixed) SPW. This is discussed in more detail in sections 3 and 6.2. We therefore use these standard deviations σ_{OH} as proxies for PW in the present paper. In a search for a possible seasonal variation of this proxy, i.e., of the PW intensity we calculate means of σ_{OH} in each month of the year. We have available 12 years of measurements of this type (OH spectrometer, 1995–2006), which yield a moderate seasonal variation. This is shown in Figure 6.

[25] The data discussed here give a climatology of σ_{OH} data. It is, however, restricted to one location. Global estimates of planetary wave intensity are given in sections 3 and 4.

3. Relative Wave Intensities

[26] We now examine the wave intensities introduced in section 2 for all months of the year. We begin by looking at traveling planetary wave intensities at the latitude and longitude (51°N, 7°E) of Wuppertal, Germany, determined from measurements of temperature at 87 km derived from OH airglow measurements at that location. These are compared with wave intensities derived from SABER measurements made at the latitude of Wuppertal. This analysis is extended to cover the altitude range from 40 to 100 km and latitudes from 20°N to 70°N in section 4.

[27] Shown in Figure 6 are the seasonal variations of the wave standard deviations at 88 km. The gravity wave variations derived from SABER (σ_{gw}) are seen to be the most intense. Their variations appear to be a mixture of annual and semiannual variation [see *Krebsbach and Preusse*, 2007]. The intensities of stationary planetary waves (σ_{spw}) are the incoherent summations of zonal wave numbers 1–4. The σ_{spw} represents lower limits but we note that the contributions from higher-wave-number SPWs are usually small. The SPW intensities are seen to be considerably smaller than those of the gravity waves in most part of the year. The SPW profile exhibits a deep minimum in summer, which is expected as planetary waves cannot exist in the easterly wind field in the summer stratosphere and mesosphere. Last we note the tidal intensities σ_{tide} are also fairly small as seen in Figure 6. They do not contribute much to the total field fluctuation. Detailed analysis (in section 4) shows that this is typical of most latitudes studied.

[28] The traveling planetary wave intensities σ_{OH} shown in Figure 6 are derived from 12 years of OH measurements and are fairly large (~6 K), the largest after gravity waves, and exhibit only a small seasonal variation. This is surprising when compared to the pronounced summer minimum of the stationary planetary waves. This effect might be due to some other wave origin such as baroclinic instability or ducting from the opposite hemisphere.

[29] If we add the variances of the four types of waves (σ_{gw}, σ_{OH}, σ_{spw}, and σ_{tide}) we obtain the variance of the total fluctuation field (σ_{sum}) as in equation (2)

$$\sigma_{sum}^2 = \sigma_{gw}^2 + \sigma_{OH}^2 + \sigma_{spw}^2 + \sigma_{tide}^2. \tag{2}$$

The variation of sum σ_{sum} is shown in Figure 6 with values ranging from 10 to 13 K. A moderate seasonal variation can be identified that has a semiannual appearance.

[30] These fluctuation sums σ_{sum} can be compared directly to the fluctuations measured by SABER (as shown in Figure 1). They are denoted σ_{sab} in Figure 6. The SABER data have been detrended for seasonal and latitudinal variations. This is because latitudinal or seasonal gradients when randomly sampled yield nonzero standard deviations

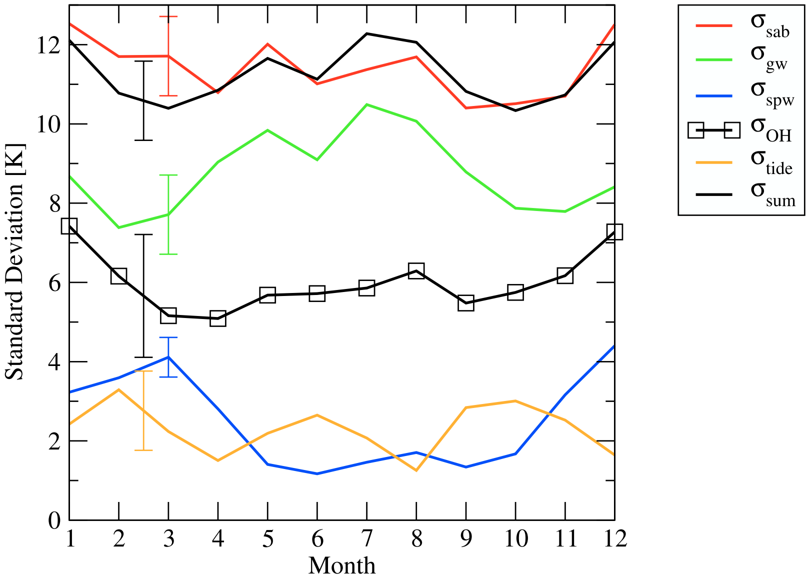

Figure 6. Comparison of four wave types during the course of the year at 88 km altitude and 50°N. Standard deviations are color coded as follows: gravity waves are green, traveling planetary waves are black with squares, stationary planetary waves are blue, and tidal waves are safran. The sum of the four waves (following equation (2)) is given in black as the root mean square σ_{sum}. It is compared to the fluctuations σ_{sab} measured by SABER (red).

even if the temperature field has no fluctuations at all. The latitudinal and seasonal gradients needed for the corrections were taken from the CIRA 1990 tables. Most of the corrections were smaller than 1 K. The σ_{sab} curve in Figure 6 is indeed close to the sum σ_{sum} as expected. Ideally these two would be identical though some deviations are expected because of interannual variations and because of different analysis periods used for the different wave types. The good agreement between σ_{sum} and σ_{sab} is encouraging, as it suggests that no major wave activity in the atmosphere has been omitted from our analysis, and the approach of equation (2) is justified. This is discussed in more detail in section 6.2.

[31] The procedure to estimate the traveling planetary wave fluctuations (σ_{OH}) cannot be applied elsewhere because there appear to be no suitable long time series of OH temperatures at locations other than Wuppertal. Therefore, it appears that comparisons as those shown in Figure 6 cannot be done elsewhere (at this altitude). However, the good agreement between σ_{sum} and σ_{sab} suggests that if we assume these are about equal everywhere that we can solve equation (1) for the traveling planetary wave fluctuations σ_{OH}. If we now call the traveling planetary wave fluctuations σ_{M} (to distinguish it from σ_{OH} derived at Wuppertal) we have

$$\sigma_{\mathrm{M}}^2 = \sigma_{\mathrm{sab}}^2 - \sigma_{\mathrm{gw}}^2 - \sigma_{\mathrm{spw}}^2 - \sigma_{\mathrm{tide}}^2. \tag{3}$$

This approach allows us to estimate σ_{M} at other altitudes and latitudes. Using SABER data from 88 km and 50°N we compare in Figure 7a σ_{M} derived from equation (3) (black squares, dashed line) with σ_{OH} (red squares, solid line) shown in Figure 6. The error bars of the σ_{OH} values are the standard deviations of the monthly values from their means over the 12 years of OH data at Wuppertal. The interannual variability of the traveling planetary waves is high. The σ_{M} values derived from equation (3) and the measured σ_{OH} agree quite well when these interannual variations are taken into account.

[32] To further confirm the approach given in Figure 6 we show in Figure 7b σ_{M} values obtained at 50°N and at 52 km altitude. At this location data from 17 years of stratospheric sounding unit (SSU) measurements taken between 1980 and 1997 at 1 hPa are available (red triangles). The Stratospheric Sounding Unit (SSU) data could not be detrended for the zonal mean temperature variations within one month and therefore have a slight high bias. Our computed σ_{M} and the observed σ_{SSU} in Figure 7b agree quite well. We will therefore use equation (3) to estimate σ_{M} as a proxy for traveling planetary waves at other latitudes and altitudes.

4. Wave Ranking

[33] A wave ranking is given in Figure 6, that is, a comparison of the relative intensities of various wave types as represented by the standard deviations of their amplitudes for 50°N and 88 km altitude. Corresponding rankings can now be established for other altitudes and latitudes since the traveling planetary waves can be estimated from equation (3). Examples are given in Figures 8a–8m showing the standard deviations of the SABER temperatures σ_{sab} on top of each picture, and below them the various waves: gravity waves σ_{gw}, traveling planetary waves σ_{M}, quasi-stationary planetary waves σ_{spw}, and tides σ_{tide}. The accuracies are believed to be similar to those given in Figure 6. (For σ_{M} see section 6.2.) The SABER standard deviations have been corrected (detrended, see section 3) for seasonal and latitudinal mean temperature variations by means of corresponding gradients taken from the CIRA 1990 tables. These corrections were rather small, and mostly much less than 1 Kelvin.

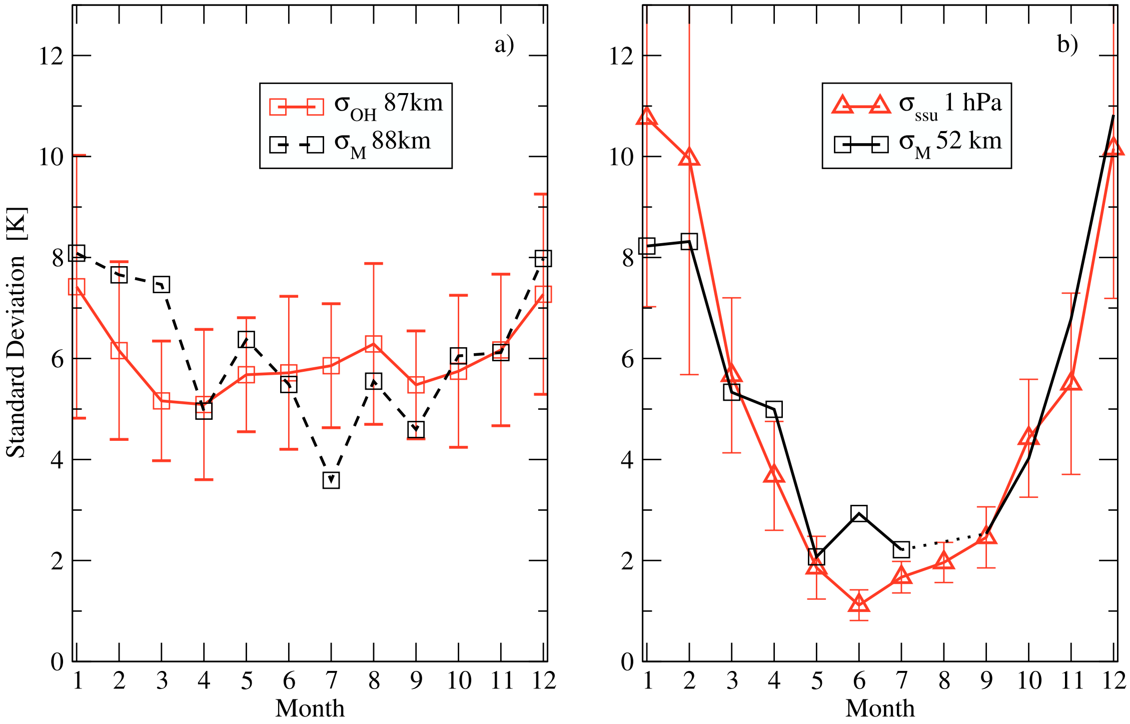

Figure 7. Measured traveling planetary waves at 50°N for (a) σ_{OH} (87 km, red) and (b) σ_{SSU} (1 hPa, red) as compared to corresponding values σ_M inferred from equation (3) at 50°N (black). See text.

[34] Figure 8 shows rankings for 20, 50, and 70°N at the altitudes of 70,80, 90, and 100 km. A number of remarkable results are seen:

[35] 1. The absolute values of the different wave amplitudes (indicated by the standard deviations) can be quite different and range from 1 (tides) to 23 K (traveling planetary waves) in Figure 8. Large variability is seen even for the same type of wave. Please note the expanded scale in Figures 8a, 8e, and 8j.

[36] 2. Gravity waves are mostly the strongest wave type (in 7 of 12 cases in Figure 8). This is, however, not the case if there are strong seasonal variations such as those that exist for the quasi-stationary and traveling planetary waves (Figures 8g, 8h, 8j, and 8m).

[37] 3. Standard deviations σ_M are derived from equation (3) and taken as proxies for traveling planetary waves. They are in second place in those cases when the gravity waves are in first place. The quasi-stationary planetary waves are fairly small on these occasions.

[38] 4. Tidal waves are mostly small except in the tropics (not shown).

[39] 5. In several cases in Figure 8 there are strong seasonal variations of one or more wave types. This especially concerns the traveling and quasi-stationary planetary waves (Figures 8e, 8g, 8h, 8j, 8l, and 8m). Planetary waves are expected to be suppressed in an easterly wind field, i.e., in summer in the stratosphere and lower mesosphere. Indeed, traveling as well as stationary planetary waves show a strong seasonal variation at 70 km and 80 km altitude and 50°N and 70°N latitude with very low values in summer and high values in winter (Figures 8g, 8h, 8l, and 8m). Corresponding curves at 50 km altitude look similar (not shown here). The swing of the seasonal variations decreases with increasing altitude. At 90 km this variation has almost disappeared and is difficult to identify (see also Figure 7a). There appears to be a "quiet layer" at this altitude which is linked to the wind reversal that occurs in summer in this regime. (At higher-altitudes winds are westerly in summer and easterly in winter.) At 100 km altitude the seasonal variation of σ_M is even reversed and shows a pronounced summer maximum and low values in winter at 70°N. This is in agreement with the wind field mentioned. It is unclear what the origin of these waves might be. The stationary planetary waves are not the reason for the shape of the σ_M profile at 100 km, 70° N, as their profile is rather unstructured and low (Figure 8j). At 50°N an inversion of the seasonal variation at 100 km is found, too (Figure 8e). It is less pronounced, but clearly the summer values (MJJ) are higher than the winter values (DJ). At either latitude winds are westerly during the summer months (MJJ) at 100 km altitude, and easterly in winter (DJ), or have a tendency to become easterly according to CIRA 1990. The σ_M values at high altitudes and high latitudes are fairly large. This is further discussed in section 6.2. Seasonal changes of gravity waves in Figure 8 indicate several annual and/or semi-annual variations that have been analyzed in detail by *Krebsbach and Preusse* [2007]. They are, however, relatively small when compared to the planetary wave seasonal variations.

[40] The σ_M values for traveling planetary waves shown in Figure 8 have also been calculated at intermediate altitudes in steps of 2 km and are given in Table 1. Vertical profiles of σ_M are therefore available from 40–100 km. Examples are shown for the months of February and July in Figure 9 for the latitudes of 70°N, 50°N, and 20°N. These two months are a good representation of winter and summer,

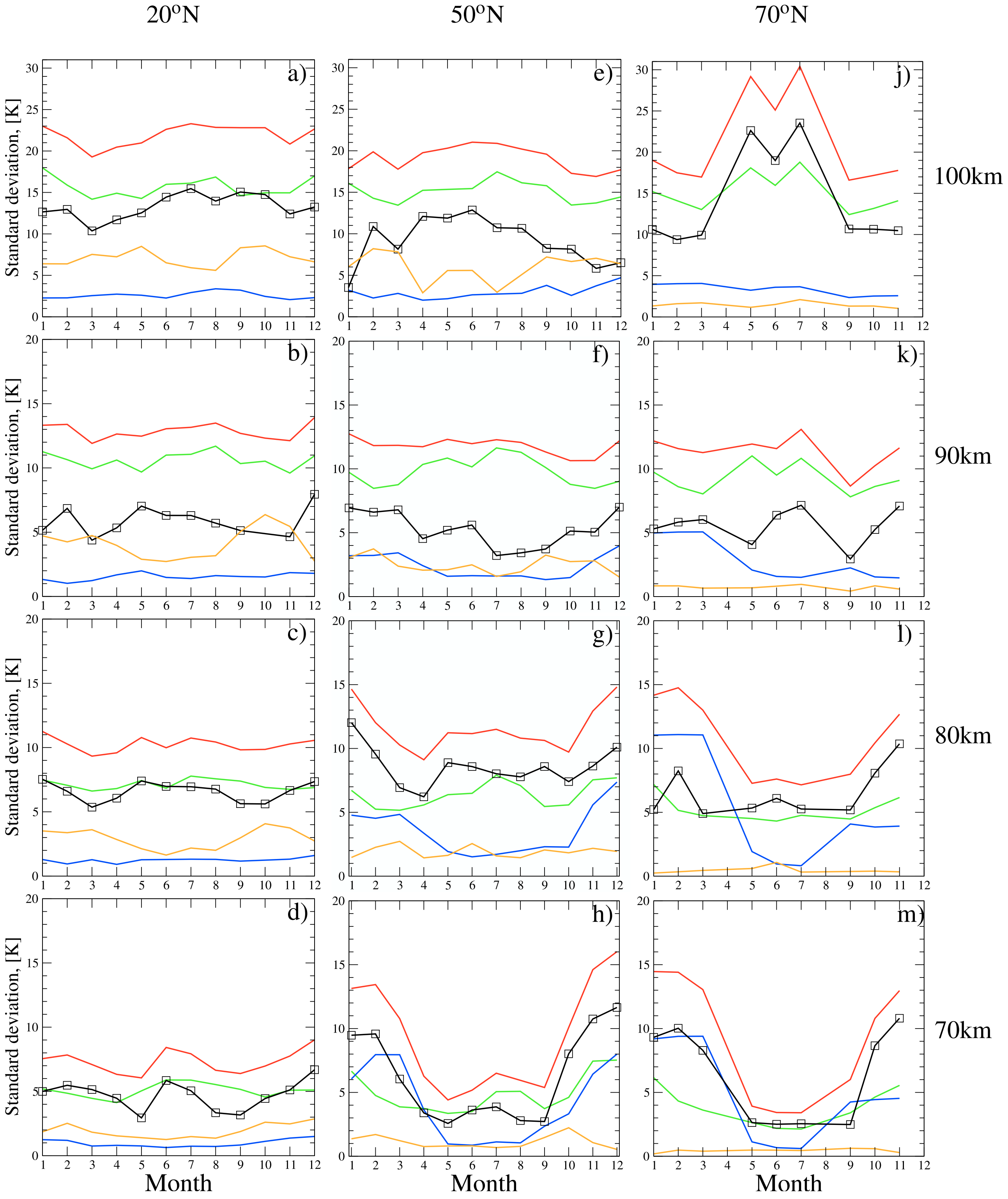

Figure 8. Wave ranking (seasonal variations) at latitudes of 20, 50, and 70°N and altitudes of 70, 80, 90, and 100 km. The four waves are gravity waves (green), traveling planetary waves (black squares), quasi-stationary planetary waves (blue), and tides (safran). Top curves are measured SABER fluctuations (red). Note the expanded scale in Figures 8a, 8e, and 8j.

respectively. Most of the σ_M profiles presented have a similar structure with a slow to moderate increase or even a decrease at the lower altitudes and a much steeper increase at altitudes above 90 km. If fitted lines would be drawn to them as in Figure 2 they would show a kink structure such as that seen in many of the other wave profiles discussed so far. The summer profile at 50°N does, however, not quite fit this picture as it has a pronounced local maximum around 80 km altitude. As

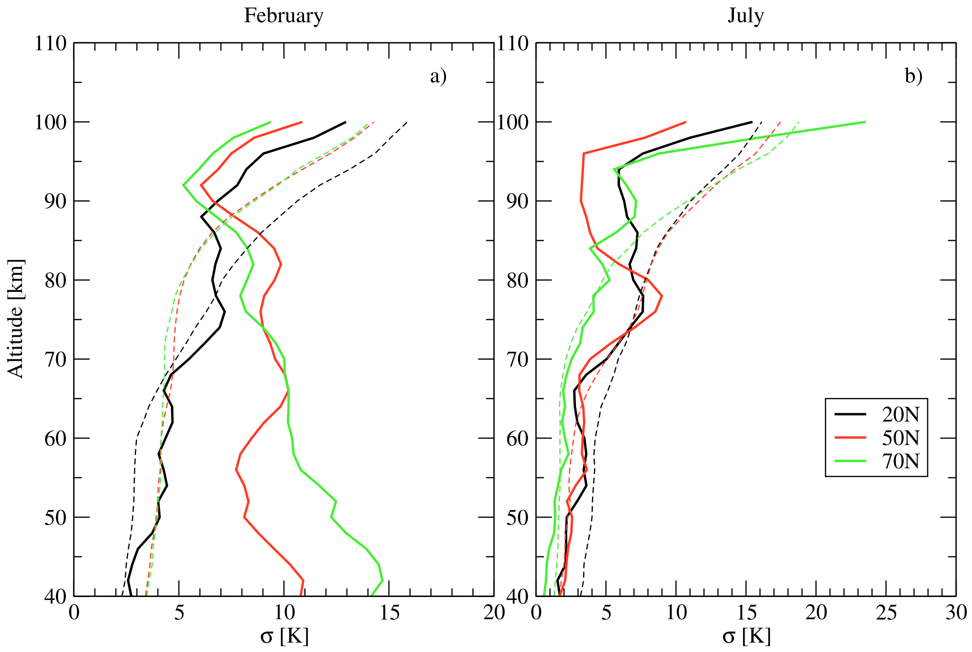

Figure 9. Vertical distributions of traveling planetary wave amplitudes (standard deviations σ_M, solid lines) for (a) February and (b) July. (Note the difference in scales.) Latitudes are 20 (black), 50 (red), and 70°N (green). Corresponding data for gravity waves taken from Figure 3 are shown for comparison (dashed lines).

gravity waves and traveling planetary waves are mostly the strongest terms in Figure 8 the gravity wave intensities from Figure 3 have been included in Figure 9 for comparison as dashed lines.

[41] The intensities of the quasi-stationary planetary waves σ_{spw} are mostly much smaller than those of the traveling planetary waves σ_M (Figure 8). The vertical profiles of the quadratic sum of the two ($\sigma_{M'}$) are therefore essentially those of the traveling planetary waves. The difference between the two is mostly less than 1 K. There are, however, exceptions as in the winter months at the lower altitudes and middle to high latitudes (Figure 8h, 8l, and 8m). To illustrate this, an example is given for February at 70°N in Figure 10, which shows $\sigma_{M'}$ as compared to σ_M. The difference is up to 7 K, but this is essentially confined to a limited altitude range (65–90 km).

[42] The corresponding gravity wave curve σ_{gw} is shown for comparison as a red line (taken from Figure 3a). The relative magnitude of the gravity waves σ_{gw} and (the sum of) the planetary waves $\sigma_{M'}$ are important for the wave turbopause. The intersection of the two curves σ_{gw} and σ_M is at the altitude z_{is}, and will be discussed in sections 5 and 6.3.

5. Formation of the Wave Turbopause

[43] The remarkable structure of the vertical profiles of standard deviations σ_{sab} (Figure 2) is a flat increase with altitude at the lower heights up to a kink, and a much steeper increase at the greater heights. In an atmosphere where the waves can freely propagate in the vertical direction, this steep increase should occur at a much lower altitude (because of energy conservation). This has been discussed in detail by *Offermann et al.* [2006a]. The flatter than expected increase has been interpreted as a consequence of wave damping at the lower altitudes in that paper. It is connected with the negative background temperature gradient in the mesosphere. At altitudes above the kink (square in Figure 2) damping is much reduced and consequently the amplitude increase is much stronger. The kink has therefore been named the wave turbopause.

[44] The altitude at which this turbopause occurs shows considerable variations with season and latitude. This has been analyzed in *Offermann et al.* [2007]. *Offermann et al.* [2006a, 2007] have presented a phenomenology of the wave turbopause and some relationship to other "turbopauses." The data shown in the present paper are meant to help regarding how the kink, i.e., the turbopause comes about.

[45] Many of the vertical intensity profiles of the different waves discussed previously in the paper show a kink-like structure themselves (e.g., Figures 3, 5, and 9). The flat (dissipation) part of the profiles at the lower altitudes is clearly seen. This means that at lower-altitudes wave damping appears to be present quite generally. It is important to notice that the superposition of two profiles each showing a kink (at different altitudes) typically yields a profile with a kink again. This results from the fact that the variances (i.e., fluctuation squares) are added and the square root of the sum is taken. In consequence the strongest part of either profile dominates the result. This applies also in case the gradient at the lower altitudes is somewhat negative as is sometimes the case with the planetary waves (Figure 9). The use of two straight fit lines further helps to identify a kink.

[46] An example for this is shown in Figure 11. Here the traveling planetary waves at high latitudes (70°N) from Figure 9a and the corresponding gravity waves from Figure 3a (also dotted lines in Figure 9a) are used. The root mean square of the two curves is calculated and shown as a blue curve in Figure 11. Linear fit lines to the lower altitudes

Table 1. Traveling Planetary Wave Activity as Derived From Equation (3)[a]

Altitude Steps (km)	Jan.	Feb.	Mar.	Apr.	May.	Jun.	Jul.	Aug.	Sep.	Oct.	Nov.	Dec.
					20°N Latitude							
40	2.80	2.74	2.91	1.93	1.71	1.74	1.71	1.46	2.24	2.93	3.25	4.03
42	3.29	2.58	2.92	2.05	1.89	1.88	1.53	1.49	2.44	2.39	3.43	3.81
44	3.65	2.78	2.83	2.36	1.85	2.06	2.11	2.16	2.34	2.56	3.64	3.93
46	3.20	3.05	3.02	2.77	2.08	2.31	2.16	2.90	2.41	2.58	3.34	3.86
48	2.88	3.73	2.95	2.86	2.16	2.61	2.15	3.49	2.37	2.63	3.25	3.64
50	2.56	4.08	3.08	2.76	2.32	2.33	2.20	3.88	2.35	2.43	2.56	3.59
52	3.43	4.02	3.24	2.89	2.37	2.69	2.93	3.93	2.45	2.73	3.01	4.06
54	4.96	4.43	3.24	2.86	2.66	3.72	3.60	4.06	2.71	3.22	3.78	4.19
56	5.08	4.27	2.94	3.06	2.73	3.65	3.41	3.66	2.56	2.71	3.36	4.13
58	4.25	4.04	2.71	2.69	2.51	3.53	3.59	3.00	2.14	2.38	3.08	4.16
60	3.93	4.37	2.61	2.91	2.75	3.58	3.45	2.95	2.10	2.53	3.02	4.73
62	3.92	4.70	2.34	2.59	2.45	3.42	2.96	2.51	1.85	2.54	3.05	5.46
64	4.00	4.68	2.31	2.72	2.36	3.42	2.78	2.30	1.60	2.46	2.77	5.59
66	3.97	4.28	2.85	2.87	2.17	3.78	2.73	2.27	1.41	2.05	3.59	5.78
68	4.10	4.62	4.02	3.48	2.20	4.58	3.58	2.53	1.90	3.00	4.81	6.14
70	5.00	5.48	5.14	4.47	2.94	5.85	5.05	3.34	3.17	4.45	5.12	6.69
72	6.55	6.23	5.81	5.46	3.50	7.01	5.89	3.95	3.77	5.06	5.36	7.23
74	7.58	6.94	6.11	5.68	4.25	7.44	6.72	4.73	4.11	4.67	7.18	7.01
76	7.80	7.18	5.83	5.46	5.86	7.65	7.62	5.71	4.90	4.55	7.54	7.56
78	7.61	6.76	5.42	5.75	7.00	7.48	7.65	6.40	5.15	5.33	6.97	7.91
80	7.53	6.60	5.36	6.06	7.40	6.97	6.95	6.77	5.63	5.61	6.66	7.36
82	7.94	6.74	5.47	6.39	7.11	6.57	6.69	7.00	6.12	5.74	6.52	7.12
84	8.12	6.99	5.45	7.01	6.63	6.37	7.15	7.52	6.21	5.57	6.66	7.18
86	7.63	6.68	5.59	7.00	6.51	6.48	7.25	7.76	6.14	5.23	6.74	7.47
88	7.04	6.07	5.24	6.31	6.94	6.47	6.50	6.99	5.74	4.30	6.05	7.61
90	5.15	6.85	4.38	5.34	7.03	6.30	6.30	5.70	5.13	0.03	4.64	7.95
92	3.21	7.78	4.92	5.06	7.38	6.31	5.91	6.59	5.10	3.66	3.69	7.50
94	4.82	8.21	5.35	6.75	7.06	7.05	5.92	7.52	6.85	7.68	4.04	8.18
96	8.13	9.02	6.39	8.05	7.25	8.99	7.63	8.37	9.25	10.11	7.22	9.40
98	10.62	11.43	7.96	10.01	9.23	11.76	11.00	10.58	11.87	12.16	10.61	10.84
100	12.65	12.96	10.36	11.70	12.53	14.43	15.46	13.96	15.05	14.74	12.41	13.24
					50°N Latitude							
40	9.32	10.80	6.63	5.30	2.28	2.08	1.69	1.29	2.87	4.56	7.98	13.78
42	10.15	10.92	6.61	5.48	2.32	2.26	2.09	0.85	2.89	4.78	8.27	14.74
44	10.82	10.30	6.08	5.28	2.31	2.62	2.17	1.00	2.90	4.61	8.18	14.89
46	10.53	9.53	5.57	5.18	2.15	2.64	2.29	0.03	2.80	4.23	7.59	14.13
48	9.55	8.78	5.13	5.07	2.20	2.84	2.52	0.82	2.81	3.87	6.81	12.60
50	8.44	8.11	5.01	4.94	2.24	3.25	2.59	1.19	2.48	3.68	6.38	11.27
52	8.23	8.32	5.33	4.99	2.07	2.93	2.21	0.03	2.53	4.02	6.79	10.83
54	7.48	8.11	5.71	5.34	2.30	3.13	2.83	1.36	3.02	4.30	7.07	9.68
56	7.09	7.73	5.60	5.09	2.75	3.65	3.63	2.24	2.73	4.20	7.09	8.43
58	7.65	7.93	5.69	4.23	2.28	3.61	3.28	1.66	2.25	4.57	7.18	8.16
60	8.38	8.46	5.95	3.72	1.98	3.33	3.34	1.93	2.29	5.00	7.11	8.12
62	8.88	9.06	6.05	3.07	1.84	3.41	3.44	1.91	1.98	5.62	7.92	8.52
64	9.70	9.84	6.27	2.40	2.09	3.42	3.37	1.73	1.55	6.38	9.08	9.12
66	10.26	10.21	6.21	1.96	1.83	3.39	3.09	1.57	1.04	7.20	10.15	10.10
68	10.15	10.06	6.07	2.30	2.17	3.36	3.11	1.75	1.16	7.73	10.60	10.81
70	9.47	9.58	6.05	3.39	2.57	3.62	3.87	2.79	2.72	8.02	10.75	11.65
72	9.44	9.35	6.17	4.41	3.51	4.13	5.35	4.28	4.46	8.25	10.44	11.85
74	9.73	9.01	6.68	5.68	4.37	5.34	7.05	5.57	6.45	8.13	9.67	11.38
76	10.42	8.89	7.08	6.40	5.91	7.09	8.52	6.69	8.15	7.93	9.34	10.78
78	11.11	9.06	6.96	6.65	7.51	8.38	8.99	7.58	8.85	7.78	8.95	10.06
80	12.02	9.56	6.93	6.21	8.89	8.58	8.02	7.78	8.59	7.40	8.62	10.10
82	12.30	9.86	6.99	5.47	9.68	8.12	5.94	7.60	7.81	7.30	8.57	10.16
84	11.13	9.53	7.23	5.33	9.54	7.02	4.39	7.61	6.74	7.20	7.95	9.48
86	9.80	8.77	7.71	5.74	8.30	5.91	3.86	6.99	5.59	6.73	7.01	8.85
88	8.09	7.66	7.47	4.96	6.38	5.49	3.59	5.55	4.59	6.05	6.12	7.98
90	6.94	6.61	6.79	4.53	5.20	5.60	3.21	3.42	3.72	5.13	5.05	7.00
92	6.03	6.06	6.23	4.76	4.47	4.20	0.03	0.03	1.55	4.30	4.37	5.08
94	6.03	6.87	6.55	5.59	5.00	4.28	0.03	2.25	2.02	4.96	4.72	4.10
96	4.31	7.50	6.78	6.48	6.32	7.42	3.41	3.81	2.63	6.71	6.04	5.04
98	0.03	8.59	7.54	8.86	9.25	10.35	7.78	6.64	5.90	7.00	5.46	4.85
100	3.52	10.88	8.14	12.09	11.88	12.86	10.73	10.66	8.25	8.15	5.83	6.52
					70°N Latitude							
40	7.66	14.16	8.36	-	0.81	0.88	0.57	-	0.03	5.87	6.00	-
42	9.94	14.70	7.97	-	0.94	1.06	0.72	-	0.03	6.02	6.12	-
44	11.27	14.52	7.22	-	1.08	1.56	0.77	-	0.41	6.07	6.45	-
46	11.62	13.92	6.85	-	0.93	1.48	0.94	-	1.02	6.13	7.15	-
48	10.54	12.95	6.22	-	1.11	1.75	1.30	-	0.03	5.62	7.52	-

Table 1. (continued)

Altitude Steps (km)	Jan.	Feb.	Mar.	Apr.	May.	Jun.	Jul.	Aug.	Sep.	Oct.	Nov.	Dec.
50	9.87	12.25	5.72	-	1.26	1.43	1.37	-	0.03	5.20	7.93	-
52	10.27	12.48	6.98	-	1.25	1.62	1.33	-	0.03	5.55	8.76	-
54	10.23	11.68	7.77	-	1.17	1.79	1.57	-	0.03	5.32	8.58	-
56	10.77	10.80	8.25	-	1.28	1.99	1.80	-	0.03	5.06	8.23	-
58	11.66	10.46	8.79	-	1.98	2.46	2.33	-	0.77	5.44	8.19	-
60	12.32	10.39	9.35	-	1.37	2.07	2.08	-	1.52	6.03	8.38	-
62	12.61	10.19	9.59	-	1.09	1.92	1.86	-	1.23	6.69	8.46	-
64	12.87	10.22	9.39	-	0.67	1.77	2.08	-	0.63	7.38	8.34	-
66	12.38	10.22	9.08	-	1.33	1.75	1.95	-	1.14	7.79	8.39	-
68	10.82	10.03	8.63	-	1.93	2.15	2.19	-	1.59	8.13	9.29	-
70	9.31	10.03	8.29	-	2.63	2.51	2.55	-	2.48	8.66	10.81	-
72	8.10	9.62	7.79	-	3.16	3.10	3.16	-	2.73	9.26	12.28	-
74	6.70	9.01	7.27	-	3.62	3.52	3.34	-	3.65	9.30	12.19	-
76	4.48	8.19	6.23	-	4.24	4.52	4.12	-	4.64	8.92	11.38	-
78	3.76	7.93	5.39	-	5.12	5.27	4.09	-	5.30	8.55	10.57	-
80	5.21	8.24	4.90	-	5.33	6.10	5.26	-	5.19	8.07	10.36	-
82	6.87	8.55	5.28	-	5.83	6.32	4.74	-	5.07	7.86	10.26	-
84	6.75	8.26	5.43	-	4.60	4.44	3.86	-	5.01	7.47	9.65	-
86	6.21	7.74	5.76	-	3.65	4.60	5.71	-	4.77	7.05	8.90	-
88	5.60	6.78	5.81	-	3.49	5.84	7.04	-	4.15	6.27	8.19	-
90	5.30	5.83	6.03	-	4.07	6.37	7.15	-	2.94	5.24	7.09	-
92	5.30	5.22	5.99	-	3.51	6.47	6.46	-	2.54	4.68	6.73	-
94	6.42	5.95	6.27	-	4.51	7.37	5.58	-	4.06	5.70	7.05	-
96	6.98	6.61	6.12	-	8.76	10.48	8.78	-	6.48	7.08	7.51	-
98	7.18	7.60	7.30	-	14.74	14.82	15.90	-	8.68	8.55	8.36	-
100	10.62	9.38	9.93	-	22.62	18.97	23.54	-	10.68	10.65	10.47	-

[a] Temperature standard deviations in Kelvin. For accuracies see section 6.2.

(40–75 km) and higher altitudes (above 90 km) are also included (black solid and dashed lines). The kinked structure is clearly visible. It is to be remembered that the measured fluctuation intensity σ_{sab} is the square root of the sum of the variances of all waves involved. It was shown in sections 2, 3, and 4 that the major contributors to the σ_{sab} profiles are the gravity waves and the traveling planetary waves (Figures 3 and 9), which mostly have kinked vertical profiles. Figure 2 can thus be explained in principle.

[47] Figure 11 suggests that the altitude of this turbopause is essentially determined by the relationship between gravity waves and planetary waves. The intersection point (Figure 10)

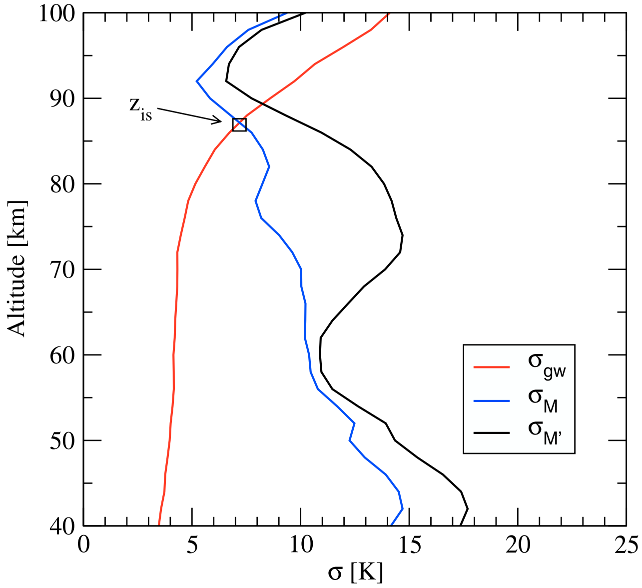

Figure 10. Comparison of traveling planetary waves σ_M with the (quadratic) sum of stationary and traveling planetary waves $\sigma_{M'}$. The corresponding gravity wave profile σ_{gw} is also shown. The intersection altitude is z_{is}. Data are for February at 70°N.

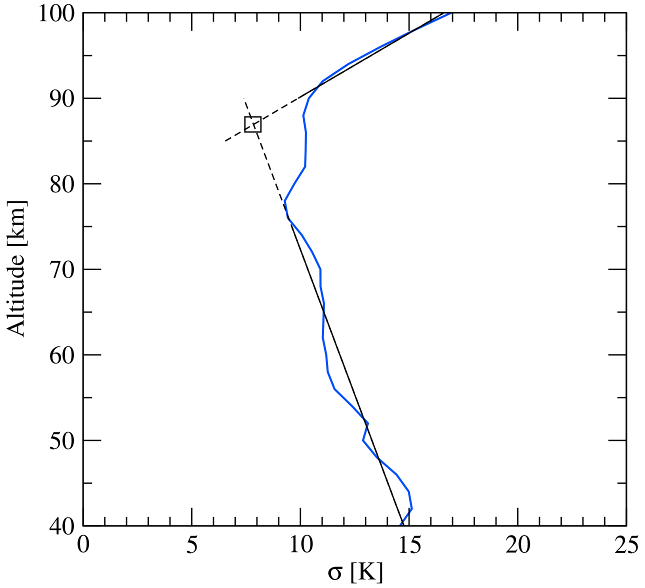

Figure 11. A kinked curve (blue) resulting from the (quadratic) superposition of gravity waves and traveling planetary waves, computed as sqrt($\sigma_{gw}^2 + \sigma_M^2$). Data shown are for 70°N and February. The black lines are linear fits to the lower and upper parts (see text).

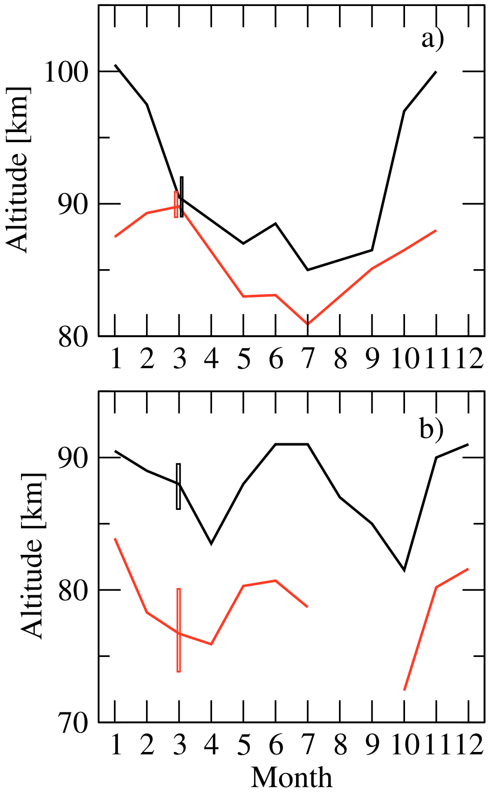

Figure 12. Seasonal variation of the altitude of intersection points z_{is} (from profiles σ_{gw} and σ'_M, see text). Red curves are for (a) 70 and (b) 20°N. Corresponding altitudes of the wave turbopause are shown for comparison (black curves, taken from *Offermann et al.* [2007, Figure 6]).

of the two profiles that are the basis of Figure 11 is near to their kink altitude (Figure 11) and hence to the turbopause altitude. An increase of planetary wave intensity in its lower part would shift the intersection point and hence the turbopause altitude to greater heights, and vice versa. Changes in the gravity wave profile would have corresponding consequences. Comparison of gravity waves and planetary waves in Figure 9 shows that the variability of intensity is much larger for the planetary waves than for the gravity waves. This suggests that a major part of the altitude variations of the turbopause (section 6.3 [*Offermann et al.*, 2006a, 2007]) is due to changes in planetary waves.

[48] To check these ideas we have determined the intersection points z_{is} of all monthly gravity and planetary wave intensity profiles in the way sketched in Figure 10. In order to take also into account the quasi-stationary planetary waves we use now the (quadratic) sum of σ_M and σ_{spw} and denote it $\sigma_{M'}$. The results for the new altitudes z_{is} are shown in Figure 12a for 70°N and in Figure 12b for 20°N. The bars shown with the March values are typical and give the changes of z_{is} that result if one of the temperature profiles (σ_{gw} or σ'_M) is shifted to higher/lower values by 1 K. At the low latitudes the altitude profiles become quite similar at low altitudes. Hence an intersection is sometimes difficult to define. These months (August, September) have been omitted from Figure 12b. For comparison the altitudes of the wave turbopause are taken from *Offermann et al.* [2007] and are also shown in Figure 12. The intersection altitudes are 5–10 km lower than the turbopause altitudes but they show a very similar seasonal variation. We therefore conclude that both gravity waves and planetary waves are the basic contributors to the formation of the wave turbopause.

6. Discussion

6.1. Potential Energy Density

[49] The deviations from the means of temperature T′ and wind speed u′ and v′ cannot only be used for fluctuation analyses. Beyond that they have frequently been used in the literature to estimate the potential and kinetic energy densities of waves in the middle atmosphere. The energy densities per unit mass are given by equations (4a) and (4b), respectively [e.g., *Tsuda et al.*, 2000],

$$E_{pot} = 1/2(g/N)^2(T'/T)^2(\text{Joule/kg}) \tag{4a}$$

$$E_{kin} = 1/2\left(u'^2 + v'^2\right)(\text{Joule/kg}), \tag{4b}$$

where T is the mean temperature, and N is the Brunt-Vaisala frequency.

[50] In the present paper we mostly use the basic measurement parameter T′ and not the derived quantity E_{pot}. This is because for the potential energy in equations (4a) we need a climatology of the mean temperature T, and for N we need a mean vertical temperature gradient. If we wanted to use equations (4a) for the various waves discussed in the present paper, it would not be clear which T climatology applies. Using SABER derived mean temperature is not as straight forward as one might expect because of asynoptical satellite sampling. (It may, for instance, contain tidal signatures; see *Oberheide et al.* [2003] for a detailed discussion.) Although it is not believed that different climatologies of temperature available from different measurements are very different today, using the directly measured fluctuations appeared to be somewhat safer. (There are other publications that also use the fluctuations instead of the energy densities [see, e.g., *Dowdy et al.*, 2007, and references therein].)

[51] The third term in equations (4a), i.e., $(T'/T)^2$, is the relative temperature variance $\sigma^2(T)$. Hence the square root of the potential energy density is approximately proportional to the standard deviation σ of the temperature fluctuations used in this paper (normalized by T). The summations according to equations (1) and (2) therefore are essentially the summations of potential energies, and the wave rankings given in Figures 6 and 8 are rankings according to the (square root of the) potential energy density (at and below 100 km).

[52] To illustrate this we pick a few examples from the literature. *Wilson et al.* [1991] present 4 years (1986–1989) of gravity wave potential energy densities from lidar data at 44° N, 6°E in France (OHP). Their upper altitude range is 60–75 km where an annual and semiannual change are seen [*Wilson et al.*, 1991, Figure 9]. This compares well with the corresponding gravity wave curve in Figure 8h. *Wilson et al.* [1991, Figure 16] give an annual mean for the potential energy density of about 105 J/kg in the altitude regime 60–75 km (Station OHP). We compare this with our 70 km

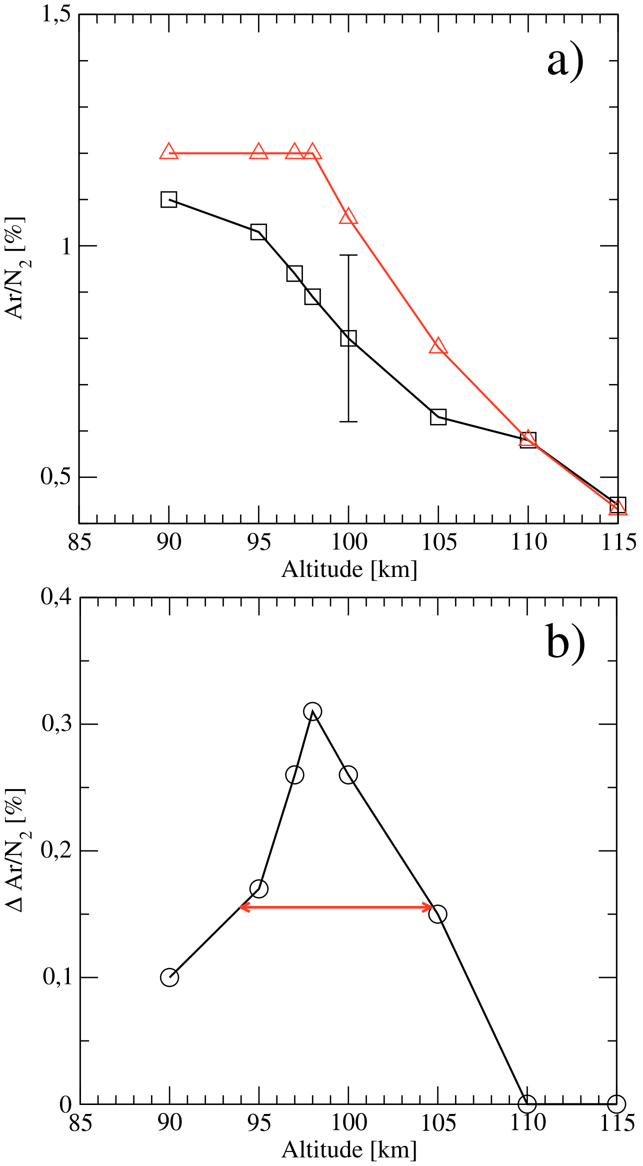

Figure 13. Ar/N$_2$ ratios as measured by mass spectrometers. (a) Measured data (black with squares) as compared to a constructed profile showing homogeneous mixing below 98 km (z_0) and diffusive separation above (red with triangles). (b) Difference of the two curves in Figure 13a. Distribution full width at half maximum is 11 km (red arrow).

GW data (Figure 8h, 4.8 K). We estimate the Brunt-Vaisala frequency by means of temperatures and temperature gradients taken from *Rees* [1990, Table 5.1] (i.e., CIRA 1986). The resulting potential energy density is 62 J/kg. This is not too far away and appears compatible with the differences of the data in altitude and latitude (not shown here).

[53] Another set of 10 years of lidar data is presented by *Sica and Argall* [2007] (43°N, 81°W). They derive kinetic energy densities for gravity waves at different altitudes. For the upper mesosphere (60–80 km) they present the following seasonal variation (in mJ/m^3, their Table 1): DJF 5.6; MAM 13.8; JJA 14.8; SON 12.0. The corresponding annual mean is 11.7 mJ/m^3. This seasonal variation is fairly different from that shown in Figure 8h. However, neither variation is really strong. The annual mean of 11.7 mJ/m^3 is converted to 158 J/kg by means of the atmosperic density at 50°N, 70 km altitude as taken from *NOAA* [1976] (i.e., USSA76). Our corresponding annual mean is $T' = 4.8$ K in Figure 8h which means a potential energy density of 62 J/kg as shown above. This is considerably smaller than the value of Sica and Argall. However, *Tsuda et al.* [2000] have pointed out that the kinetic energy density should be larger than the potential energy density by a factor of 5/3 to 2. Some part of the difference could also be due to the difference of the two data sets in latitude and especially in altitude. It should also be remembered that the GW climatology used here does not include vertical wavelengths below 5 km while the latter are included in the lidar based analysis. *Manson et al.* [1981] (52°N, 107°W) derived kinetic energy densities from radar measurements of the wind components u' and v' according to equation (4b). They obviously, however, omitted the factor 1/2 in the equation. They give kinetic energy densities of two types of gravity waves at 80 km and 97 km, respectively (their Figure 13). The seasonal variations shown are – in their relative values – quite similar to our data in Figures 8g and 8e. We estimate the approximate annual mean from their Figure 13 to be 5 mJ/m^3 at 80 km and 0.7 mJ/m^3 at 97 km. Our corresponding values for the potential energy density from Figure 8 are 2.2 mJ/m^3 (80 km) and 0.25 mJ/m^3 (100 km), respectively. This is lower by factors 2.3–2.8. Taking into account the above mentioned factor 1/2 and a factor 5/3 cited by *Tsuda et al.* [2000] our values should be lower by a factor 3.3, which is not too far away. (For these comparisons we have again used temperatures, temperature gradients, and densities from *Rees* [1990, Table 5.1] and *NOAA* [1976].)

[54] A more recent paper [*Dowdy et al.*, 2007] gives gravity wave kinetic energy densities from radar wind measurements at Arctic and Antarctic latitudes (more than 5 years). We use here only the Arctic data from the stations of Poker Flat (65°N, 147°W) and Andenes (69°N, 16°E) and compare them to our 70°N data. *Dowdy et al.* [2007] find considerable seasonal variations with basically an annual and a semiannual component that, however, strongly depend on altitude and gravity wave period. The general behavior is similar to what we see in our Figure 8. The best agreement is obtained for the station of Andoya which is nearest to our latitude of 70°N (their Figure 8, long gravity wave periods). *Dowdy et al.* [2007] give summer and winter mean data in their Figure 6. We use their Andoya data (70–100 km) to compare with our gravity wave February and July data shown in Figure 9. *Dowdy et al.* [2007] use the wind variances as a measure of the kinetic energy density, i.e., they do not apply the factor 1/2 in equation (4b). The energy densities are strongly altitude dependent in either data set. The ratio of the Andoya data to those presented here is 1.9 in winter (range 1.5 to 2.4 for the different altitudes) and 2.4 in summer (range 0.83 to 6.2). Hence a very approximate agreement is obtained similar to the lower latitudes [*Manson et al.*, 1981] considering the factor 1/2 and the Tsuda factors cited (resulting in an expected ratio of about 4). We have compared the energy densities from the same measurement technique and different latitudes (at 80 km altitude, annual mean). From the radar techniques we

obtain 5mJ/m^3 at 52°N [*Manson et al.*, 1981] and 2.4 mJ/m^3 at 69°N [*Dowdy et al.*, 2007]. This is a factor 2.1 decrease within a 17° increase in latitude. The present SABER data (Figures 8 and 9) yield 2.2 mJ/m^3 at 50°N and 1.5 mJ/m^3 at 70°N, i.e., a factor 1.5 decrease for a 20° latitude increase.

[55] In summary the SABER energy densities shown here are lower by a factor 1.7 to 2.8 than the data taken from the literature. All of these literature values, except *Wilson et al.* [1991], are, however, kinetic energy densities. Before they can be compared to potential energy densities they apparently need a down correction of a factor of 2 or more (see above and *Tsuda et al.* [2000]). The data of *Wilson et al.* [1991] are potential energies and a factor 1.7 higher than our data. This difference may be due to differences in latitude and/or altitude as mentioned above. Interannual and long-term changes could also play a role. In addition to the already mentioned omission of short vertical wavelength GWs in the SABER climatology, the inherent horizontal smoothing of the limb scan technique may also play a role.

6.2. Traveling Planetary Waves

[56] A climatology of traveling planetary waves (PW) is not yet available at present. We therefore present our σ_M values as a proxy for planetary wave intensities. But, we also need to estimate how reliable this parameter is; i.e., whether this proxy is contaminated for any reason. There are a number of possible contamination sources,which we discuss herein.

6.2.1. Gravity Waves

[57] In our discussion of Figure 6 we argued that gravity waves do not influence the σ_M proxy much because of spatial and temporal filtering. This may be questionable for larger-scale (inertial) gravity waves. We therefore used OH measurements from a second (twin) station that is operated at the Observatory of Hohenpeissenberg (48°N, 11°E) some 360 km away from Wuppertal, to look for simultaneous large-scale gravity waves over the two stations and found very few. These two stations are in completely different gravity wave environments as the high mountains of the Alps are very near to Hohenpeissenberg. Hence we would expect to see differences in σ_M at the two stations if their measurements were noticeably influenced by gravity waves. We found a mean difference on the order of 3% over several years (to be published in a forthcoming paper). We therefore conclude that the gravity wave influence on σ_M might be of this order of magnitude, which is small. Another argument in support of this conclusion is derived from the seasonal variations of σ_{GW} and σ_M illustrated in Figure 6. If there was considerable gravity wave influence on σ_M, the two curves should show some similarities, but they do not. The correlation coefficient is -0.03. The same argument holds for the corresponding curves in Figure 8, which are also fairly dissimilar. We therefore tentatively conclude that gravity waves in general have little influence on σ_M.

6.2.2. Tides

[58] In Figure 6 the tidal values are considerably smaller than σ_M. If some fraction of these tides should contribute to σ_M this contribution would be fairly small because of the quadratic summation. Also the seasonal curves should show some similarity, which is not the case. Similarly, in Figure 8, σ_M is for the most part much larger than σ_{tide}, except in Figure 8b and 8e. However, the dissimilarity of the curves makes it again unlikely that the tides would influence σ_M.

6.2.3. Stationary Planetary Waves

[59] As mentioned in section 2.4, these waves are undetectable in the OH measurements. However, SPW are frequently only quasi-stationary. That is, their amplitudes build up or dissipate, or their positions shift (for instance in the east–west direction). Such events may appear to be traveling planetary waves. Similar features are seen during major and minor stratospheric warmings, vacillations, and other kinds of SPW modulations. It is long and well known that large-scale SPW changes/variations occur in the stratosphere [e.g., *Leovy et al.*, 1985]. *Oberheide et al.* [2006b] found similar structures in the mesosphere. The mesospheric structures appear to be smaller, but whether this difference is typical remains unknown. An estimate for SPW changes in the mesosphere can be inferred from Figure 8. At most altitudes and latitudes σ_{SPW} is considerably smaller than σ_M, and hence the quasi-stationary waves cannot contribute significantly to σ_M. However, at lower altitudes and middle to high-latitudes σ_{spw} are comparatively large, and change rapidly (Figures 8h, 8l, and 8m). The largest time change (decay) in this picture is seen in Figure 8l, where σ_{SPW} decays here by 4.6 K per month over about two months. In a single month (for instance in April), this is equivalent to a standard deviation of 1.4 K and hence to a wavelike oscillation with 2 K amplitude. In comparison, $\sigma_M = 5$ K in April, corresponding to an amplitude of 7.1 K. The quadratic sum of these two amplitudes is 7.4 K; σ_M is changed by less than 4%. Hence the SPW changes seen in Figure 8 do not generally contribute much to σ_M.

[60] As concerns major stratospheric warmings their activity has been comparatively small during the 2002–2005 time window of our analysis [e.g., *Labitzke et al.*, 2005]. Mesospheric signatures of stratospheric warmings are much weaker than they are in the stratosphere, and may even appear as mesospheric coolings [e.g., *Offermann et al.*, 1987]. We have checked the major warming periods cited by *Labitzke et al.* [2005] in our 87 km OH temperatures and found no abnormal level of planetary wave activity during any of these times.

[61] Atmospheric vacillations are disturbances in high-latitude winter that are also capable of contaminating our σ_M proxy. Stratospheric normal modes may be forced by the interaction of planetary waves with the mean flow, or by spontaneous internal instabilities [e.g., *Christiansen*, 1999; *Scott and Haynes*, 2000, see also references therein]. Time scales are of the order of a few days to several weeks, which are on the order of disturbances discussed herein. Stratospheric warmings have also been discussed in terms of vacillations. Vacillations analyses have focused on stratospheric and lower mesospheric altitudes. The events appear to be small in the middle mesosphere to lower thermosphere.

[62] Transient disturbances of stationary planetary waves could quite generally contaminate our traveling planetary wave proxy σ_M (Figure 8 and Table 1). Experimental knowledge about such temperature disturbances in the mesosphere is limited, because it is difficult to distinguish between disturbed/modulated SPW and traveling PW. This distinction can be achieved if the vertical phase structure of the waves is determined, requiring a large number of vertical temperature profile measurements (for instance by

rocket flights or lidar soundings). *Bittner et al.* [1994], *Bittner* [1993], *Offermann et al.* [1987], and *Scheer et al.* [1994] reported about two northern winter campaigns with very many soundings of this kind (i.e., DYANA Campaign, MAP/WINE Campaign). They determined the vertical phase structure of the waves and thus identified several SPW modulations that otherwise would have been mistaken as traveling PW. We have used 260 data points between 40 and 87 km at 69°N and 44°N during several months of winters 1990 and1983–1984 from these campaigns to estimate the contamination of our proxy σ_M in Figure 8 and Table 1. Several minor stratospheric warmings occurred during this time, along with a major warming in February 1984. The result of our analysis including all disturbances is as follows: 85% of the data points showed a relatively small contamination of σ_M (i.e., changes between 0% and 20%). In 15% of the cases the disturbance of σ_M was stronger: 20–65%. It thus follows that σ_M is a fairly reliable parameter with moderate contamination. (N.B., We used counting statistics to generate the contamination numbers above. Average contamination values would be smaller.) We also addressed the question as to whether a plausible long-term trend in σ_M might invalidate our supporting analyses of 15–20 year old campaign data. Specifically, we analyzed 87 km altitude measurements and did not find a significant trend in the 1995 to 2004 time interval [*Offermann et al.*, 2006b].

[63] Referring to travelling planetary waves as σ_M in the following, some of the intensities σ_M in Figure 8 need a more detailed discussion. The σ_M values at high altitudes and latitudes are fairly large. Especially the values in Figure 8j (70°N, 100 km) show a strong summer maximum with values up to 23 K, with a relatively flat minimum superimposed in June. The question arises whether this feature is real. To estimate the accuracy of the σ_M curve we refer to Figure 7, which compares two inferred σ_M curves with two measured ones. These are at mid latitude (50°N), and at low altitude (52 km) and high altitude (88 km), respectively. The largest differences between the measured and the inferred curves are 2.5 K or less. We tentatively adopt this value also as the accuracy at high latitudes and altitudes (Figure 8j). In consequence the summer maximum can be taken as real. This is not so clear for the flat June relative minimum. It is about 4 K deep, which is just within two times 2.5 K. Its reality may thus be questionable. However, the two independent curves for σ_{gw} and σ_{sab} both show a similar June minimum, and something comparable is seen in Figure 8k. It may therefore be well possible that the minimum is a true atmospheric feature. Pronounced traveling planetary waves at high altitudes have been found many years ago in ionospheric data [e.g., *Takahashi et al.*, 2006; *Lawrence and Jarvis*, 2003, and references therein]. Corresponding oscillations in the neutral atmosphere have been observed in upper mesosphere/lower thermosphere (UMLT) winds on many occasions [e.g., *Murphy et al.*, 2007; *Takahashi et al.*, 2006; *Lawrence and Jarvis*, 2003, and references therein]. Planetary wave oscillations in UMLT temperatures have been inferred from OH Meinel band emissions at 87 km altitude. Maximum amplitudes of 10–15 K have been observed [e.g., *Scheer et al.*, 1994; *Murphy et al.*, 2007]. Meteor temperatures have shown planetary wave type oscillations with amplitudes on the order of 10 K in the 85–95 km range [*Kirkwood et al.*, 2002]. Temperature information at higher altitudes on planetary waves are sparse. *Riggin et al.* [2006] have analyzed SABER temperature measurements up to 110 km. They identified 5-day planetary waves with amplitudes larger than 12 K near 100 km. Amplitudes were maximized in summer, with a relative minimum right in the middle of summer. Corresponding model calculations (Thermosphere-Ionosphere-Mesosphere-Electrodynamics General Circulation Model (TIME GCM)) showed amplitudes up to 16 K. A similar model analysis of a 6.5 day planetary wave showed a relative minimum in the middle of summer [*Liu et al.*, 2004, see also references therein].

[64] In summary large amplitude planetary waves at high altitudes/high latitudes are well known. Temperature amplitudes, however, that have been measured so far are not as high as indicated in Figure 8j. However, gravity wave intensities in this picture are also very high, and in comparison the indicated planetary wave intensities appear not at all impossible.

[65] A special aspect needs to be noted that follows from the way we infer the traveling wave intensities (σ_M): The standard deviation σ_M in Figure 8 results from the difference of the measured σ_{sab} and the other wave intensities. If any of the latter should be biased low, in consequence σ_M would be biased high. The quasi-stationary planetary waves σ_{spw} –as an example, are quite low in Figures 8e, 8f, 8j, and 8k (below 4–5 K). Substantially higher values have been observed in measurements, as for instance by *Steinbrecht et al.* [2007] who saw a quasi-stationary wave of 12 K amplitude at 87 km altitude and 50°N latitude. As the seasonal analysis of quasi-stationary planetary waves used here is based on a data set of 1-year duration only, a possible low bias cannot be excluded. Furthermore, tidal activity at middle to high latitudes may differ from the GSWM simulations used here. The recent SABER tidal temperature climatology [*Forbes et al.*, 2008] shows that a number of nonmigrating tidal components peak at or poleward of 40° latitude. This is only partly reflected in the GSWM simulations that do not include tidal components forced by nonlinear wave-wave interaction. The net effect on the inferred traveling planetary waves needs to be further investigated in the future but it is rather unlikely that it will remove the summer maximum in σ_M.

6.3. Turbopause Altitude/Turbopause Layer

[66] As already mentioned the wave turbopause is defined as the kink in the vertical fluctuation profiles σ_{sab}. Such kinks are also found on many occasions for various wave types (Figures 3, 5, and 9). In Figure 10 the flat parts of the gravity and planetary wave profiles (i.e., at the lower altitudes) indicate wave damping and the altitude range where it occurs. If, on the one hand, the flat part of the planetary wave profile is increased to a higher intensity this is interpreted as higher wave activity accompanied by higher dissipation (turbulence). At the same time intersection altitude z_{is} and turbopause altitude are increased. If, on the other hand, the flat part of the gravity wave profile is extended to higher altitudes this means increased wave dissipation at these higher altitudes. Also in this case the intersection point and hence the turbopause is shifted upward. Hence in our interpretation, in either case high wave dissipation corresponds to a high wave turbopause altitude.

[67] The seasonal variation of the turbopause altitude at 20°N shows a combination of an annual and a semiannual variation (Figure 12b, black curve). This is found in a very similar way at 50°N (Figure 6 [*Offermann et al.*, 2007]). Corresponding eddy diffusion coefficients have been derived from radar measurements at 52°N in the upper mesosphere [*Manson et al.*, 1981]. Their seasonal variation shows one maximum in winter and another one in summer. It is thus very similar to our variations of the turbopause altitudes. A very similar seasonal variation is observed in the OH* emission intensities (D. Offermann, unpublished data, 2006) that are the basis for derivation of the OH temperatures at 51°N in Figure 6. It suggests variations of vertical transports of trace constituents. The three results (turbopause, eddy diffusion, OH* emission intensities) thus appear to be manifestations of the same dynamical feature in the mesosphere and lower thermosphere.

[68] As it is conceivable that the transition between damped and undamped wave propagation will not occur at a single altitude, it is reasonable to assume that the turbopause forms a vertically extended layer rather than a two-dimensional surface. This is in parallel to the lower atmosphere where the tropopause is nowadays discussed as a transition layer a few kilometers thick in the vertical [e.g., *Engel et al.*, 2006, and references therein]. It is important to mention that the turbopause was discussed years ago in terms of a transition region [e.g., *Hocking*, 1990].

[69] We have performed an analysis of the variation of the wave turbopause altitude in winter (February) at 50°N. The turbopause layer was found to be about 8 km thick (i.e., plus/minus one standard deviation of the mean turbopause altitude at a weekly time resolution). In summer (July) this layer thickness is somewhat smaller. At higher latitudes (70°N) the corresponding values are somewhat larger.

[70] To evaluate this, we analyzed a limited set of measurements by rocket-borne mass spectrometers that are available at around 40°N (various times of the year [*Offermann et al.*, 1981]). Even though these are old data they are nevertheless among the best we presently have: in that paper eight measurements are collected that took place right in the altitude regime where the turbopause is expected. The mass spectrometers measured number densities of Argon and Nitrogen, and hence the Ar/N_2 ratio can be used as a proxy for the Ar mixing ratio.We have reanalyzed these data. The Ar/N_2 ratio in the lower atmosphere (homosphere) is 0.012. The altitude at which the ratio deviates from this value is called the homopause z_0 (Figure 13).

[71] The individual Ar/N_2 profiles of the eight flights show strong fluctuations. It is therefore difficult to assign individual homopauses to the flights. Hence the range of homopause altitudes, i.e., the thickness of the homopause layer (turbopause layer) cannot be derived. Therefore we have taken another approach. The Ar/N_2 columns between 95 and 115 km have been calculated by *Offermann et al.* [1981] and have been found to efficiently smooth the individual fluctuations. These columns are a measure of the homopause height, i.e., the larger the Ar/N_2 column, the higher the homopause height. (If in Figure 13a the red curve (triangles) is shifted to higher altitudes this means a corresponding shift of the homopause and an increase of the column between 95 and 105 km. See below.) The column variability can therefore be used to estimate the homopause variability. A layer thickness (2σ) of about 8 km is obtained this way. This value is the same as the layer thickness found above for the wave turbopause (note the 10° latitude difference). The exact agreement must be fortuitous, albeit remarkable, because the wave turbopause shows considerable seasonal variations which presumably are not well sampled by the eight rocket flights.

[72] If the atmosphere is in diffusive equilibrium above the homopause (first approximation) the Ar/N_2 vertical profile can be calculated once the homopause altitude z_0 is given [e.g., *Offermann et al.*, 1981]. The mean profile of the eight measured Ar/N2 profiles has been calculated and is shown in Figure 13a (black curve with squares). The vertical scatter bar at 100 km is the standard deviation, and is typical of the other altitudes. A diffusive equilibrium profile is also shown (red curve, triangles) for which a tentative homopause at 98 km was chosen. This choice was taken because the two curves coincide at the highest altitudes (110–115 km). This is interpreted such that at and above these altitudes the measured data are essentially in diffusive equilibrium. At the lower altitudes the mean measured curve is, however, found to substantially deviate from the diffusion equilibrium. The difference of the two curves is shown in Figure 13b. The deviation profile shows a sharp peak which should, of course, not be taken too serious considering the error bars shown. The vertical range of the deviation is estimated to be about 11 km (full width at half maximum, 94–105 km, red bar with arrows in Figure 13b). The deviation is believed to be due to neutral turbulence. If turbulence stops at the homopause it decays above that level, and its action will be felt over some distance called "the mixing length Λ." The range of deviation from diffusive equilibrium thus results from the combination of turbopause (homopause) variations and the mixing length. The homopause variations are estimated by the turbopause layer of 8 km. We tentatively assume a linearly combined action of the turbopause layer with the mixing length Λ to form the 11 km deviation range. From this we estimate the mixing length Λ to be 3 km (order of magnitude).

[73] The seasonal mean of the wave turbopause at 40°N is taken from *Offermann et al.* [2007] (Figure 6) and is found to be at 91.5 km. The corresponding wave turbopause layer depth is about 8 km, i.e., it extends from about 88 km to 96 km. (The same layer depth as at 50°N has been used here.) The extension of the turbopause layer derived from the mass spectrometer data is 94–102 km. These two layers have considerable overlap and hence the turbopauses of the two techniques should not be far apart.

[74] The combination of the turbopause layer thickness and mixing length Λ yields a fairly extended reach of turbulent impact. Many different methods have been used in the past to determine the turbopause altitude, and quite different altitudes have been obtained [e.g., *Offermann et al.*, 2007, and references therein]. Part of these discrepancies may be due to this large reach of turbulent impact.

7. Conclusions

[75] Temperature standard deviations from zonal mean values are used in the middle atmosphere as a proxy for atmospheric wave activity. Temperature fluctuations are

analyzed for the major wave types in the northern mesosphere and lower thermosphere, and a wave ranking is obtained, to our knowledge, for the first time. The ranking shows some dependence on latitude and altitude (20–70°N, 70–100 km). In most cases gravity waves play a major role at these moderate to high latitudes. Traveling planetary waves are in second place, and stationary planetary waves and tidal waves yield a lesser contribution. (The latter are not measured but come from a model simulation.)

[76] Temperature variances are closely related to potential energy density of the atmosphere. Gravity wave energy densities are compared to several examples given in the literature. Reasonable agreement is obtained, with our data being somewhat lower. This may be due to the fact that the SABER limb scan measurements cannot determine the short wavelength gravity waves. In most of the paper we use temperature standard deviations rather than energy densities to characterize the waves as calculation of these densities requires climatologies of temperature and Brunt-Vaisala frequencies that are not always at hand.

[77] On the basis of the wave ranking an estimation of traveling planetary wave intensities is attempted. A wave proxy is derived. It indicates a first and preliminary climatology of wave dependence on altitude and latitude. Possible contaminations of the proxy are discussed, and are found to be relatively moderate. Proxy values at high altitudes/high latitudes are rather large and might indicate an underestimation of other wave types here (stationary planetary waves, tides).

[78] The concept of a wave turbopause has been developed in earlier publications [*Offermann et al.*, 2006a, 2007] on the basis of vertical profiles of temperature fluctuations and a kink or bend in the profiles (change of gradient) in the upper mesosphere. This concept is further analyzed here. Kinks are found in the intensity profiles of many atmospheric wave types. All these waves appear to experience strong damping of some kind in the lower part of the middle atmosphere and much reduced damping in its uppermost part.

[79] The latter is presumably linked to the strong temperature increase at the base of the thermosphere. Seasonal and latitudinal variations of the turbopause height (kink altitude) have been described by *Offermann et al.* [2006a, 2007]. In the present analysis we find that these variations mostly result from changes of the relative intensities of gravity waves and planetary waves. This result leads to the concept of a turbopause layer rather than a surface as the waves are highly variable. A layer thickness of 8 km is estimated from the data. The value is confirmed by an earlier set of rocket-borne mass spectrometer measurements. The latter data indicate that their turbopause altitude appears to be rather near to that of the wave turbopause. The mass spectrometer data also suggest that above the homopause there is a mixing layer with a thickness (mixing length) of about 3 km.

[80] The total reach of turbulent impact is therefore quite substantial (order 11 km) and may explain why previous measurements have yielded highly different turbopause altitudes. All of these turbulence results are coarse estimates.

[81] **Acknowledgments.** This work was supported by Deutsche Forschungsgemeinschaft (DFG, Bonn) as part of the CAWSES priority program. We acknowledge the support of the German Climate Computing Centre (DKRZ, Hamburg) where the HAMMONIA simulations were performed. J. M. F. acknowledges support under grant NNX07AB74G from the NASA TIMED Program. D.O. thanks Ralf Koppmann for continuous discussions and support.

References

Beig, G., et al. (2003), Review of mesospheric temperature trends, *Rev. Geophys.*, *41*(4), 1015, doi:10.1029/2002RG000121.

Bittner, M. (1993), Langperiodische temperaturoszillationen in der unteren und mittleren atmosphäre (0–100 km) während der DYANA kampagne, Ph.D. thesis, Univ. of Wuppertal, Wuppertal, Germany.

Bittner, M., et al. (1994), Long period/large scale oscillations of temperature during the DYANA campaign, *J. Atmos. Sol. Terr. Phys.*, *56*, 1675–1700, doi:10.1016/0021-9169(94)90004-3.

Bittner, M., D. Offermann, and H. H. Graef (2000), Mesopause temperature variability above a midlatitude station in Europe, *J. Geophys. Res.*, *105*(D2), 2045–2058, doi:10.1029/1999JD900307.

Bittner, M., D. Offermann, H.-H. Graef, M. Donner, and K. Hamilton (2002), An 18-year time series of OH rotational temperatures and middle atmosphere decadal variations, *J. Atmos. Sol. Terr. Phys.*, *64*, 1147–1166, doi:10.1016/S1364-6826(02)00065-2.

Chanin, M. L., A. Hauchecorne, and N. Smires (1990), Contribution to a new reference atmosphere from ground-based lidar, *Adv. Space Res.*, *10*(12), 211–216, doi:10.1016/0273-1177(90)90398-J.

Christiansen, B. (1999), Stratospheric vacillations in a General Circulation Model, *J. Atmos. Sci.*, *56*, 1858–1872, doi:10.1175/1520-0469(1999)056<1858:SVIAGC>2.0.CO;2.

Cole, A. E., and A. J. Kantor (1978), Air Force reference atmospheres, *Rep. AFGL-TR-78-0051*, Air Force Geophys. Lab., Hanscom Air Force Base, Mass.

Dowdy, A. J., R. A. Vincent, M. Tsutsum, K. Igarashi, Y. Murayama, W. Singer, and D. J. Murphy (2007), Polar mesosphere and lower thermosphere dynamics: 1. Mean windsand gravity waves climatologies, *J. Geophys. Res.*, *112*, D17104, doi:10.1029/2006JD008126.

Eckermann, S. D., and P. Preusse (1999), Global measurements of stratospheric mountain waves from space, *Science*, *286*, 1534–1537.

Engel, A., et al. (2006), Highly resolved observations of trace gases in the lowermost stratosphereand upper troposphere from the SPURT project: An overview, *Atmos. Chem. Phys.*, *6*, 283–301.

Ern, M., P. Preusse, P. Alexander, and C. D. Warner (2004), Absolute values of gravity wave momentum flux derived from satellite data, *J. Geophys. Res.*, *109*, D20103, doi.:10.1029/2004JD004752.

Ern, M., P. Preusse, and C. D. Warner (2006), Some experimental constraints for spectral parameters used in the Warner and McIntyre parameterization scheme, *Atmos. Chem. Phys.*, *6*, 4361–4381.

Fetzer, E. J., and J. Gille (1994), Gravity wave variance in LIMS temperatures, part 1: Variability and comparison with background winds, *J. Atmos. Sci.*, *51*, 2461–2483, doi:10.1175/1520-0469 (1994)051<2461:GWVILT>2.0.CO;2.

Fleming, E. L., S. Chandra, J. J. Barnett, and M. Corney (1990), Zonal mean temperature, pressure, zonal wind and geopotential height as functions of latitude, *Adv. Space Res.*, *10*(12), 11–59, doi:10.1016/0273-1177 (90)90386-E.

Forbes, J. M., X. Zhang, S. Palo, J. Russell, C. J. Mertens, and M. Mlynczak (2008), Tidal variability in the ionospheric dynamo region, *J. Geophys. Res.*, *113*, A02310, doi.:10.1029/2007JA012737.

Hagan, M. E., and J. M. Forbes (2002), Migrating and nonmigrating diurnal tides in the middle and upper atmosphere excited by tropospheric latent heat release, *J. Geophys. Res.*, *107*(D24), 4754, doi:10.1029/2001JD001236.

Hagan, M. E., and J. M. Forbes (2003), Migrating and nonmigrating semidiurnal tides in theupper atmosphere excited by tropospheric latent heat release, *J. Geophys. Res.*, *108*(A2), 1062, doi:10.1029/2002JA009466.

Hagan, M. E., M. D. Burrage, J. M. Forbes, J. Hackney, W. J. Randel, and X. Zhang (1999), GSWM-98: Results for migrating solar tides, *J. Geophys. Res.*, *104*, 6813–6828, doi:10.1029/1998JA900125.

Hall, C. M., C. E. Meek, A. H. Manson, and S. Nozawa (2008), Turbopause determination, climatology, and climatic trends using medium frequency radars at 52°N and 70°N, *J. Geophys. Res.*, *113*, D13104, doi:10.1029/2008JD009938.

Hedin, A. E. (1983), A revised thermospheric model based on mass spectrometer and incoherent scatter data: MSIS-83, *J. Geophys. Res.*, *88*, 10,170–10,188, doi:10.1029/JA088iA12p10170.

Hocking, W. K. (1990), Turbulence in the region 80–120 km, *Adv. Space Res.*, *10*, 153–161, doi:10.1016/0273-1177 (90)90394-F.

Kirkwood, S., V. Barabash, B. U. E. Brändström, A. Moström, K. Stebel, N. Mitchell, and W. Hocking (2002), Noctilucent clouds, PMSE and 5-day planetary waves: A case study, *Geophys. Res. Lett.*, *29*(10), 1411, doi:10.1029/2001GL014022.

Krebsbach, M., and P. Preusse (2007), Spectral analysis of gravity wave activity in SABER temperature data, *Geophys. Res. Lett.*, *34*, L03814, doi:10.1029/2006GL028040.

Labitzke, K., B. Naujokat, and M. Kunze (2005), The lower arctic stratosphere in winter since 1952: An update, *Stratospheric Processes Role Clim. Newsl.*, *24*, 27–28.

Lawrence, A. R., and M. J. Jarvis (2003), Simultaneous observations of planetary waves from 30 to 220 km, *J. Atmos. Sol. Terr. Phys.*, *65*, 765–777, doi:10.1016/S1364-6826 (03)00081-6.

Leovy, C. B., C.-R. Sun, M. H. Hitchman, E. E. Remsberg, J. M. Russell III, L. L. Gordley, J. C. Gille, and L. V. Lyjak (1985), Transport of ozone in the middle stratosphere: Evidence for planetary wave breaking, *J. Atmos. Sci.*, *42*, 230–244, doi:10.1175/1520-0469 (1985)042<0230:TOOITM>2.0.CO;2.

Liu, H.-L., E. R. Talaat, R. G. Roble, R. S. Lieberman, D. M. Riggin, and J.-H. Yee (2004), The 6.5-day wave and its seasonal variability in the middle and upper atmosphere, *J. Geophys. Res.*, *109*, D21112, doi:10.1029/2004JD004795.

Manson, A. H., C. E. Meek, and J. B. Gregory (1981), Winds and waves (10 min–30 days) in the mesosphere and lower thermosphere at Saskatoon (52°N, 107°W, L = 4.3) during the year, October 1979 to July 1980, *J. Geophys. Res.*, *86*, 9615–9625, doi:10.1029/JC086iC10p09615.

Mertens, C. J., M. G. Mlynczak, M. López-Puertas, P. P. Wintersteiner, R. H. Picard, J. R. Winick, L. L. Gordley, and J. M. Russell III (2001), Retrieval of mesospheric and lowerthermospheric kinetic temperature from measurements of CO_2 15 μm Earth limb emission under non-LTE conditions, *Geophys. Res. Lett.*, *28*(7), 1391–1394, doi:10.1029/2000GL012189.

Mertens, C. J., et al. (2004), SABER observations of mesospheric temperatures and comparisons with falling sphere measurements taken during the 2002 summer MaCWAVE campaign, *Geophys. Res. Lett.*, *31*, L03105, doi:10.1029/2003GL018605.

Murphy, D. J., W. J. R. French, and R. A. Vincent (2007), Long-period planetary waves in the mesosphere and lower thermosphere above Davis, Antarctica, *J. Atmos. Sol. Terr. Phys.*, *69*(17–18), 2118–2138, doi:10.1016/j.jastp.2007.06.008.

NOAA (1976), U.S. Standard Atmosphere 1976, *Tech. Rep. NOAA-S/T 76-1562*, Washington, D. C.

Oberheide, J., M. E. Hagan, and R. G. Roble (2003), Tidal signatures and aliasing in temperature data from slowly precessing satellites, *J. Geophys. Res.*, *108*(A2), 1055, doi:10.1029/2002JA009585.

Oberheide, J., D. Offermann, J. M. Russell III, and M. G. Mlynczak (2006a), Intercomparison of kinetic temperature from 15 μm CO_2 limb emissions and OH* (3,1) rotational temperature in nearly coincident air masses: SABER, GRIPS, *Geophys. Res. Lett.*, *33*, L14811, doi:10.1029/2006GL026439.

Oberheide, J., H.-L. Liu, O. A. Gusev, and D. Offermann (2006b), Mesospheric surf zone and temperature inversion layers in early November 1994, *J. Atmos. Sol. Terr. Phys.*, *68*, 1752–1763, doi:10.1016/j.jastp.2005.11.013.

Offermann, D., V. Friedrich, P. Ross, and U. von Zahn (1981), Neutral gas composition measurements between 80 and 120 km, *Planet. Space Sci.*, *29*, 747–764, doi:10.1016/0032-0633 (81)90046-5.

Offermann, D., R. Gerndt, R. Küchler, K. Baker, W. R. Pendleton, W. Meyer, U. von Zahn, C. R. Philbrick, and F. J. Schmidlin (1987), Mean state and long term variations of temperature in the winter middle atmosphere above northern Scandinavia, *J. Atmos. Sol. Terr. Phys.*, *49*, 655–674, doi:10.1016/0021-9169 (87)90011-0.

Offermann, D., M. Jarisch, J. Oberheide, O. Gusev, I. Wohltmann, J. M. Russell III, and M. G. Mlynczak (2006a), Global wave activity from upper stratosphere to lower thermosphere: A new turbopause concept, *J. Atmos. Sol. Terr. Phys.*, *68*, 1709–1729, doi:10.1016/j.jastp.2006.01.013.

Offermann, D., M. Jarisch, M. Donner, W. Steinbrecht, and A. I. Semenov (2006b), OH temperature re-analysis forced by recent variance increases, *J. Atmos. Sol. Terr. Phys.*, *68*, 1924–1933, doi:10.1016/j.jastp.2006.03.007.

Offermann, D., M. Jarisch, H. Schmidt, J. Oberheide, K.-U. Grossmann, O. Gusev, J. M. Russell III, and M. G. Mlynczak (2007), The "wave turbopause", *J. Atmos. Sol. Terr. Phys.*, *69*, 2139–2158, doi:10.1016/j.jastp.2007.05.012.

Picone, J. M., A. E. Hedin, D. P. Drob, and A. C. Aikin (2002), NRLMSISE-00 empirical model of the atmosphere: Statistical comparisons and scientific issues, *J. Geophys. Res.*, *107*(A12), 1468, doi:10.1029/2002JA009430.

Preusse, P., S. D. Eckermann, J. Oberheide, M. E. Hagan, and D. Offermann (2001), Modulation of gravity waves by tides as seen in CRISTA temperatures, *Adv. Space Res.*, *27*, 1773–1778, doi:10.1016/S0273-1177 (01)00336-2.

Preusse, P., A. Dörnbrack, S. D. Eckermann, M. Riese, B. Schaeler, J. Bacmeister, D. Broutman, and K. U. Grossmann (2002), Space based measurements of stratospheric mountain waves by CRISTA: 1. Sensitivity, analysis method, and a case study, *J. Geophys. Res.*, *107*(D23), 8178, doi:10.1029/2001JD000699.

Preusse, P., et al. (2006), Tropopause to mesopause gravity waves in August: Measurement and modeling, *J. Atmos. Sol. Terr. Phys.*, *68*, 1730–1751.

Preusse, P., S. D. Eckermann, and M. Ern (2008), Transparency of the atmosphere to short horizontal wavelength gravity waves, *J. Geophys. Res.*, *113*, D24104, doi:10.1029/2007JD009682.

Preusse, P., S. D. Eckermann, M. Ern, J. Oberheide, R. H. Picard, R. G. Roble, M. Riese, J. M. Russell III, and M. G. Mlynczak (2009), Global ray tracing simulations of the SABER gravity wave climatology, *J. Geophys. Res.*, doi:10.1029/2008JD011214, in press.

Ramaswamy, V., et al. (2001), Stratospheric temperature trends: Observations and model simulations, *Rev. Geophys.*, *39*, 71–122, doi:10.1029/1999RG000065.

Rees, D. (Ed.) (1990), *COSPAR International Reference Atmosphere: 1986, Part II: Middle Atmosphere Models*, *Adv. Space Res.*, vol. 10, Elsevier, New York.

Riggin, D. M., et al. (2006), Observations of the 5-day wave in the mesosphere and lower thermosphere, *J. Atmos. Sol. Terr. Phys.*, *68*, 323–339, doi:10.1016/j.jastp.2005.05.010.

Scheer, J., E. R. Reisin, J. P. Espy, M. Bittner, H. H. Graef, D. Offermann, P. P. Ammosov, and V. M. Ignatyev (1994), Large-scale structures in hydroxyl rotational temperatures during DYANA, *J. Atmos. Terr. Phys.*, *56*, 1701–1715, doi:10.1016/0021-9169 (94)90005-1.

Schmidt, H., G. P. Brasseur, M. Charron, E. Manzini, M. A. Giorgetta, T. Diehl, V. I. Fomichev, D. Kinnison, D. Marsh, and S. Walters (2006), The HAMMONIA chemistry climate model: Sensitivity of the mesopause region to the 11-year solar cycle and CO_2 doubling, *J. Clim.*, *19*, 3903–3931, doi:10.1175/JCLI3829.1.

Scott, R. K., and P. H. Haynes (2000), Internal vacillations in stratosphere-only models, *J. Atmos. Sci.*, *57*, 3233–3250, doi:10.1175/1520-0469 (2000)057<3233:IVISOM>2.0.CO;2.

Sica, R. J., and P. S. Argall (2007), Seasonal and nightly variations of gravity-wave energy density in the middle atmosphere measured by the Purple Crow Lidar, *Ann. Geophys.*, *25*, 2139–2145.

Smith, S. A., D. C. Fritts, and T. E. Vanzandt (1987), Evidence for a saturated spectrum of atmospheric gravity waves, *J. Atmos. Sci.*, *44*, 1404–1410, doi:10.1175/1520-0469 (1987)044<1404:EFASSO>2.0.CO;2.

Steinbrecht, W., P. Winkler, and D. Offermann (2007), Temperaturschwankungen und Planetare Wellen in der Mittlere Atmosphäre, *Ozonbull. 115*, Deutsch. Wetterdienstes, Offenbach, Germany.

Takahashi, H., C. M. Wrasse, D. Pancheva, M. A. Abdu, I. S. Batista, L. M. Lima, P. P. Batista, B. R. Clemesha, and K. Shiokawa (2006), Signatures of 3–6 day planetary waves in the equatorial mesosphere and ionosphere, *Ann. Geophys.*, *24*(12), 3343–3350.

Tsuda, T., M. Nishida, C. H. Rocken, and R. H. Ware (2000), A global morphology of gravity wave activity in the stratosphere revealed by the GPS occultation data (GPS/MET), *J. Geophys. Res.*, *105*, 7257–7273, doi:10.1029/1999JD901005.

Wilson, R., M. L. Chanin, and A. Hauchecorne (1991), Gravity waves in the middle atmosphere observed by Rayleigh lidar: 2. Climatology, *J. Geophys. Res.*, *96*, 5169–5183, doi:10.1029/90JD02610.

Wu, D. L., and J. W. Waters (1996), Satellites observations of atmospheric variances: A possible indication of gravity waves, *Geophys. Res. Lett.*, *23*, 3631–3634, doi:10.1029/96GL02907.

M. Donner, Donner Tontechnik, Gerstau 6, Remscheid D-42857, Germany.

J. M. Forbes, Aerospace Engineering Sciences, University of Colorado, Boulder, CO 80309-0429, USA.

O. Gusev, J. Oberheide, and D. Offermann, Physics Department, University of Wuppertal, Gaußstrasse 20, Wuppertal D-42097, Germany. (offerm@uni-wuppertal.de)

M. Hagan, High Altitude Observatory, NCAR, P.O. Box 3000, Boulder, CO 80307-3000, USA.

M. G. Mlynczak, NASA Langley Research Center, Hampton, VA 23681-2199, USA.

P. Preusse, Institut für Chemie und Dynamik der Geosphäre I: Stratosphäre, Forschungszentrum Jülich, Wilhelm-Johnen-Strasse, D-52425 Jülich, Germany.

J. M. Russell III, Center for Atmospheric Sciences, Hampton University, Hampton, VA 23668, USA.

H. Schmidt, Max Planck Institute for Meteorology, Bundesstrasse 53, Hamburg D-20146, Germany.